INVITED PAPER

Silicon-Integrated High-Density Electrocortical Interfaces

This paper examines the state of the art of chronically implantable electrocorticography (ECoG) interface systems and introduces a novel modular ECoG system using an encapsulated neural interfacing acquisition chip (ENIAC) that allows for improved, broad coverage in an area of high spatiotemporal resolution.

By Sohmyung Ha, *Member IEEE*, Abraham Akinin, *Student Member IEEE*, Jiwoong Park, *Student Member IEEE*, Chul Kim, *Student Member IEEE*, Hui Wang, *Student Member IEEE*, Christoph Maier, *Member IEEE*, Patrick P. Mercier, *Member IEEE*, and Gert Cauwenberghs, *Fellow IEEE*

ABSTRACT | Recent demand and initiatives in brain research have driven significant interest toward developing chronically implantable neural interface systems with high spatiotemporal resolution and spatial coverage extending to the whole brain. Electroencephalography-based systems are noninvasive and cost efficient in monitoring neural activity across the brain, but suffer from fundamental limitations in spatiotemporal resolution. On the other hand, neural spike and local field potential (LFP) monitoring with penetrating electrodes offer higher resolution, but are highly invasive and inadequate for long-term use in humans due to unreliability in long-term data recording and risk for infection and inflammation. Alternatively, electrocorticography (ECoG) promises a minimally invasive, chronically implantable neural interface with resolution and spatial coverage capabilities that, with future technology scaling, may meet the needs of recently proposed brain initiatives. In this paper, we discuss the challenges and state-of-the-art technologies that are enabling next-generation fully implantable high-density ECoG interfaces, including details on electrodes, data acquisition front-ends, stimulation drivers, and circuits and antennas for wireless communications and power delivery. Along with state-of-the-art implantable ECoG interface systems, we introduce a modular ECoG system concept based on a fully encapsulated neural interfacing acquisition chip (ENIAC). Multiple ENIACs can be placed across the cortical surface, enabling dense coverage over wide area with high spatiotemporal resolution. The circuit and system level details of ENIAC are presented, along with measurement results.

KEYWORDS | BRAIN Initiative; electrocorticography; neural recording; neural stimulation; neural technology

I. INTRODUCTION

The Brain Research through Advancing Innovative Neurotechnologies (BRAIN) Initiative envisions expanding our understanding of the human brain. It targets development and application of innovative neural technologies to advance the resolution of neural recording, and stimulation toward dynamic mapping of the brain circuits and processing [1], [2]. These advanced neurotechnologies will enable new studies and experiments to augment our current understanding of the brain, thereby enabling tremendous advances in diagnosis and treatment opportunities over a broad range of neurological diseases and disorders.

Studying the dynamics and connectivity of the brain requires a wide range of technologies to address multiple temporal and spatial scales. Fig. 1 shows spatial and temporal resolutions and spatial coverage of the various brain monitoring methods that are currently available [3]–[6].

Noninvasive methods such as magnetic resonance imaging (MRI), functional magnetic resonance imaging

Manuscript received January 1, 2016; revised May 24, 2016; accepted May 30, 2016. Date of publication August 5, 2016; date of current version December 20, 2016. This work was supported by the University of California Multicampus Research Programs and Initiatives (MRPI) and the University of California San Diego Center for Brain Activity Mapping.

The authors are with the University of California San Diego, La Jolla, CA 92093-0412 USA (e-mail: soha@ucsd.edu; pmercier@ucsd.edu; gert@ucsd.edu).

Digital Object Identifier: 10.1109/JPROC.2016.2587690

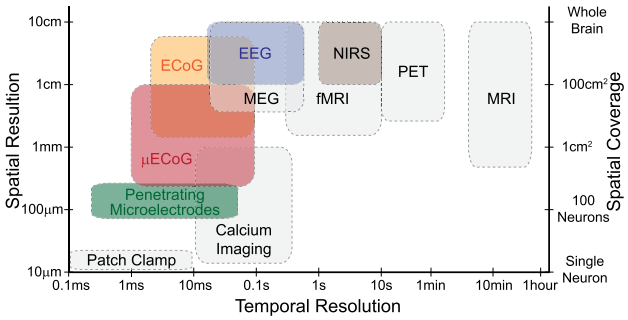

Fig. 1. ***Spatial and temporal resolution as well as spatial coverage of various neural activity monitoring modalities [3]–[5]. For each modality shown, the lower boundary of the box specifies the spatial resolution indicated on the left axis, whereas the upper boundary specifies the spatial coverage on the right axis. The width of each box indicates the typical achievable range of temporal resolution. Portable modalities are shown in color. Bridging an important gap between noninvasive and highly invasive techniques, μECoG has emerged as a useful tool for diagnostics and brain-mapping research.***

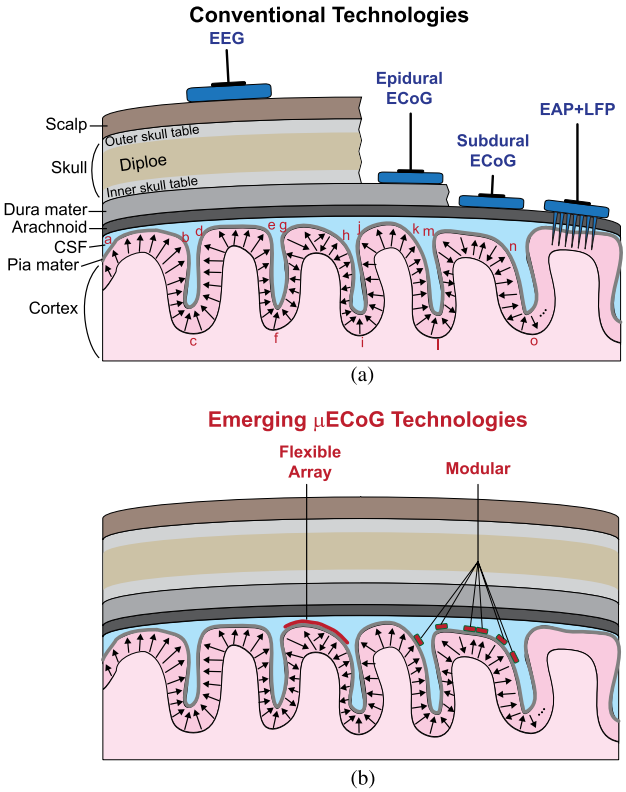

Fig. 2. ***(a) Conventional electrophysiology methods including EEG, ECoG, and neural spike and LFP recording with penetrating microelectrodes. Both EEG and ECoG can capture correlated collective volume conductions in gyri such as regions of a-b, d-e, and j-k. However, they cannot record opposing volume conductions in sulci such as regions of b-c-d and e-f-g and random dipole layers such as regions of g-h and l-m-n-o [18]. (b) Emerging fully implantable μECoG technologies enabled by flexible substrate ECoG microarrays and modular ECoG interface microsystems. Such technologies are capable of capturing local volume conducting activities missed by conventional methods, and are extendable to cover large surface area across cortex.***

(fMRI), magnetoencephalography (MEG), and positron emission tomography (PET) provide whole-brain spatial coverage. Although fMRI achieves high spatial resolution down to 1 mm, its temporal resolution is severely limited (1–10 s) as the system measures neural activity indirectly by quantifying blood oxygenation to support regions with more elevated metabolism. In contrast, MEG provides higher temporal resolution (0.01–0.1 s) at the expense of poor spatial resolution (1 cm). Whereas fMRI and MEG provide complementary performance in spatiotemporal resolution, PET offers molecular selectivity in functional imaging at the expense of lower spatial (1 cm) and temporal (10–100 s) resolution, and the need for injecting positron emitting radionuclides in the bloodstream. However, neither fMRI and MEG, nor PET are suitable for wearable or portable applications, as they all require very large, expensive, and high power equipment to support the sensors as well as extensively shielded environments.

In constrast, electrophysiology methods, which directly measure electrical signals that arise from the activity of neurons, offer superior temporal resolution. They have been extensively used to monitor brain activity due to their ability to capture wide ranges of brain activities from the subcellular level to the whole brain oscillation level as shown in Fig. 2(a). Due to recent advances in electrode and integrated circuit technologies, electrophysiological monitoring methods can be designed to be portable, with fully wearable or implantable configurations for brain–computer interfaces having been demonstrated.

One of the most popular electrophysiological monitoring methods is electroencephalography (EEG), which records electrical activity on the scalp resulting from volume conduction of coherent collective neural activity throughout the brain, as illustrated in Fig. 2(a). EEG recording is safe (noninvasive) and relatively inexpensive, but its spatiotemporal resolution is limited to about 1 cm and 100 Hz, due largely to the dispersive electrical properties of several layers of high-resistive tissue, particularly skull, between the brain and the scalp. In contrast, recording with intracranial brain-penetrating microelectrodes [labeled as EAP + LFP in Fig. 2(a)] can achieve much higher resolution due to the much closer proximity to individual neurons. Thus, it is also widely used for brain research and brain–computer interface (BCI) applications. Using microelectrodes, extracellular action potential (EAPs) and local field potentials (LFPs) can be recorded from multiple neurons across multiple cortical areas and layers. Even though penetrating microelectrodes can provide rich information from neurons, they can suffer from tissue damage during insertion [7]–[9],

and have substantial limitations in long-term chronic applications due to their susceptibility to signal degradation from electrode displacement and immune response against the electrodes [10]. Because of the more extreme invasiveness and longevity issues, chronic implantation of penetrating microelectrodes in humans is not yet viable.

Between the two extremes of EEG and penetrating microelectrode arrays, a practical alternative technique is electrocoticography (ECoG), or intracranial/intraoperative EEG (iEEG), which records synchronized postsynaptic potentials at locations much closer to the cortical surface, as illustrated in Fig. 2(a). Compared to EEG, ECoG has higher spatial resolution [11]–[13], higher signal-to-noise ratio, broader bandwidth [14], and much less susceptibility to artifacts from movement, electromyogram (EMG), or electrooculargram (EOG) [15], [16]. In addition, ECoG does not penetrate the cortex, does not scar, and can have superior long-term signal stability recording through subdural surface electrodes.

ECoG recording was pioneered in the 1920s by Hans Berger [17]. He recorded ECoG signals with electrodes placed on the dural surface of human patients. In the 1930s through 1950s, Wilder Penfield and Herbert Jasper at the Montreal Neurological Institute used ECoG to identify epileptogenic zones as a part of the Montreal procedure, which is a surgical protocol to treat patients with severe epilepsy by removing sections of the cortex most responsible for epileptic seizures. In addition, intraoperative electrical stimulation of the brain has been used to explore the functional mapping of the brain including brain areas for speech, motor, and sensory functions. This localization of important brain regions is important to exclude from surgical removal. Although ECoG is still the gold standard for decoding epileptic seizure foci and determining target regions for surgical removal, the role of ECoG has been reduced due to recent advances in imaging techniques for functional brain mapping such as fMRI, PET, and MEG.

With advances in high channel count and wireless operation, however, ECoG has again emerged as an important tool not only for more effective treatment of epilepsy, but also for investigating other types of brain activity across the cortical surface. ECoG recording provides stable brain activity recording at a mesoscopic spatiotemporal resolution with a large spatial coverage up to whole or a significant area of the brain. Advanced miniaturized electrode arrays have pushed the spatial resolution of ECoG recording to less than 1 mm, offering a unique opportunity to monitor large-scale brain activity much more precisely. Moreover, wireless implantable microsystems based on flexible technology or via modular placement of multichannel active devices, both illustrated in Fig. 2(b), have recently emerged as a new paradigm to record more closely to the cortical surface (in many cases on top of the pia), while enabling coverage along the natural curvature of the cortex without penetration. These micro ECoG, or μECoG, devices enable even higher spatial resolution than conventional ECoG systems, and are beginning to enable next-generation brain mapping, therapeutic stimulation, and BCI systems.

This paper discusses the challenges of designing next-generation ECoG interfaces, including recording, miniaturization, stimulation, powering, and data communications. Solutions are presented by first surveying state-of-the-art technologies, and then through a detailed exploration of a state-of-the-art modular system implementation.

II. ECoG INTERFACES: RECORDING AND STIMULATION

A. Volume Conduction With Differential Electrodes

Volume conduction of ionic currents in the body is the source of biopotentials such as EEG, ECoG, ECG, and EMG. In the frequency band of interest for biopotential recording (typically less than 1 kHz), the quasi-static electric field equations with conductivities of tissue layers are a good approximate representation [19]. To first order, a volume conducting current monopole I spreads radially through tissue with an outward current density of magnitude $I/4\pi r^2$ at distance r, giving rise to an outward electric field of magnitude $I/4\pi\sigma r^2$ and a corresponding electrical potential $I/4\pi\sigma r$, where σ is the tissue volume conductivity.

1) Differential Recording: For EEG, a current dipole as a closely spaced pair of opposing current monopoles is typically an adequate model representing distant sources of synchronous electrical activity across large assemblies of neurons or synapses [19]. In contrast, for implanted neural recording including ECoG and single-unit neural spike/LFP recording, a set of monopole currents resulting from individual neural units is a more appropriate model at the local spatial scale, especially for high density recording with electrodes spaced at dimensions approaching intercellular distances. Since the volume conducting currents from neural action potentials are spatially and temporally distributed, only a few effective current sources at a time are typically active near an electrode, one of which is illustrated in the vicinity of two closely spaced electrodes in Fig. 3(a). Furthermore, unlike the ground-referenced recording with single-ended electrodes for EEG, high-density electrode arrays typically require differential recording across electrodes, particularly in μECoG integrated recording since the miniaturized geometry does not allow for a distal ground connection.

In Fig. 3(a), the recorded differential voltage V as a function of the distances r_+ and r_- of the two electrodes

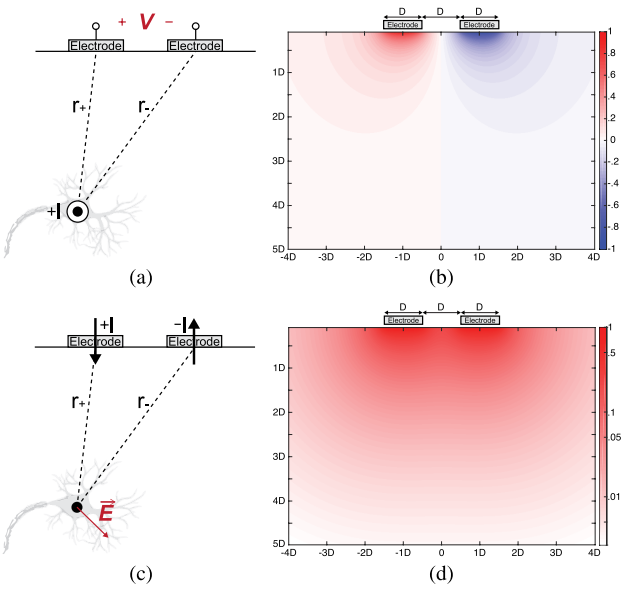

Fig. 3. ***(a) Neural recording setting with closely spaced differential electrodes interfacing below with neural tissue of volume conductivity σ. (b) Spatial map of the effect of the location of a current source $+I$ in the tissue on recorded differential voltage V, in units $1/\sigma D$. (c) Neural stimulation setting with differential currents injected into the surrounding tissue through the same two closely spaced electrodes. (d) Spatial map of the resulting electric field magnitude $|\vec{E}|$ in the tissue, in units $1/\sigma D^2$.***

from a current source I induced by the activity of adjacent neurons can be expressed as

$$V(r_+, r_-) \cong \frac{I}{2\pi\sigma}\left(\frac{1}{r_+} - \frac{1}{r_-}\right) \tag{1}$$

valid for distances r_+, r_- substantially larger than the electrode diameter D. Although the expression is similar to that for an EEG current dipole recorded with a single electrode, it is fundamentally different in that here the difference in monopole activity results from differential sensing with two closely spaced electrodes rather than from dipolar distribution of two closely spaced currents. The factor 2 rather than 4 in the denominator arises from the semi-infinite boundary conditions along the horizontal plane of the electrode substrate, in that volume conduction is restricted to the tissue below the substrate. Fig. 3(b) shows a spatial map of the effect of a current source located in tissue below the electrode pair, with electrode diameter D and pitch $2D$, on the measured differential voltage V. Its recording penetration depth is roughly $2D$, the electrode pitch, vertically, and about $4D$ horizontally. Note again that this is for a single monopolar source; in the presence of dipolar activity with two opposing nearby currents (i.e., charge balancing across a soma and dendrite of a neuron extending below the electrodes) the measured voltage (1) becomes double differential, leading to a quadrupolar response profile.

2) Differential Stimulation: The same pair of closely spaced electrodes can be used for differential stimulation by injecting currents into the surrounding tissue. Again, the absence of a distal ground connection in miniature integrated electrode arrays necessitates local charge balancing so that the currents through the two electrodes need to be of equal strength and opposing polarity, constituting a current dipole sourced within the electrode array. The resulting differential current stimulation can be modeled with the diagram shown in Fig. 3(c). The current dipole from the pair of differential stimulation currents flowing through the two electrodes induces an electrical field $\vec{\mathbf{E}}$ in the brain tissue expressed by

$$\vec{\mathbf{E}}(r_+, r_-) \cong \frac{I}{2\pi\sigma}\left(\frac{\vec{\mathbf{u}}_{r_+}}{r_+^2} - \frac{\vec{\mathbf{u}}_{r_-}}{r_-^2}\right) \tag{2}$$

where again $r_+, r_- \gg D$, and $\vec{\mathbf{u}}_{r_+}$ and $\vec{\mathbf{u}}_{r_-}$ represent unit vectors pointing outwards along the direction of r_+ and r_-, respectively. With the same electrode configuration of Fig. 3(b), the magnitude of the electric field $|\vec{\mathbf{E}}|$ is shown in Fig. 3(d) indicating a shallow region near the electrodes being electrically stimulated. Note that the electrical field for stimulation is inversely proportional to the square of distance to each electrode, while the potential measured for recording is inversely proportional to linear distance. Thus, the available depth of differential stimulation is shallower than that of differential recording. In general, the penetration depth of stimulation and recording are roughly a few times larger than the electrode pitch.

3) Electrode Array Configurations: While this is a simplified model, it is sufficiently representative to demonstrate the effectiveness of differential electrode configurations for both recording and stimulation without a global reference, as required for fully integrated μECoG in absence of a distal ground connection. As the analysis and simulations above show, the spatial response of differential recording and stimulation are quite localized near the electrode sites, on a spatial scale that matches the electrode dimensions and spacing. Thus, aside from spatial selection of recording or stimulation along the 2-D surface by translation of selected pairs of adjacent electrodes, depth and spatial resolution of recording or stimulation can be controlled via virtual electrode pitch, by pooling multiple electrodes in complementary pairs of super electrodes at variable spacing between centers.

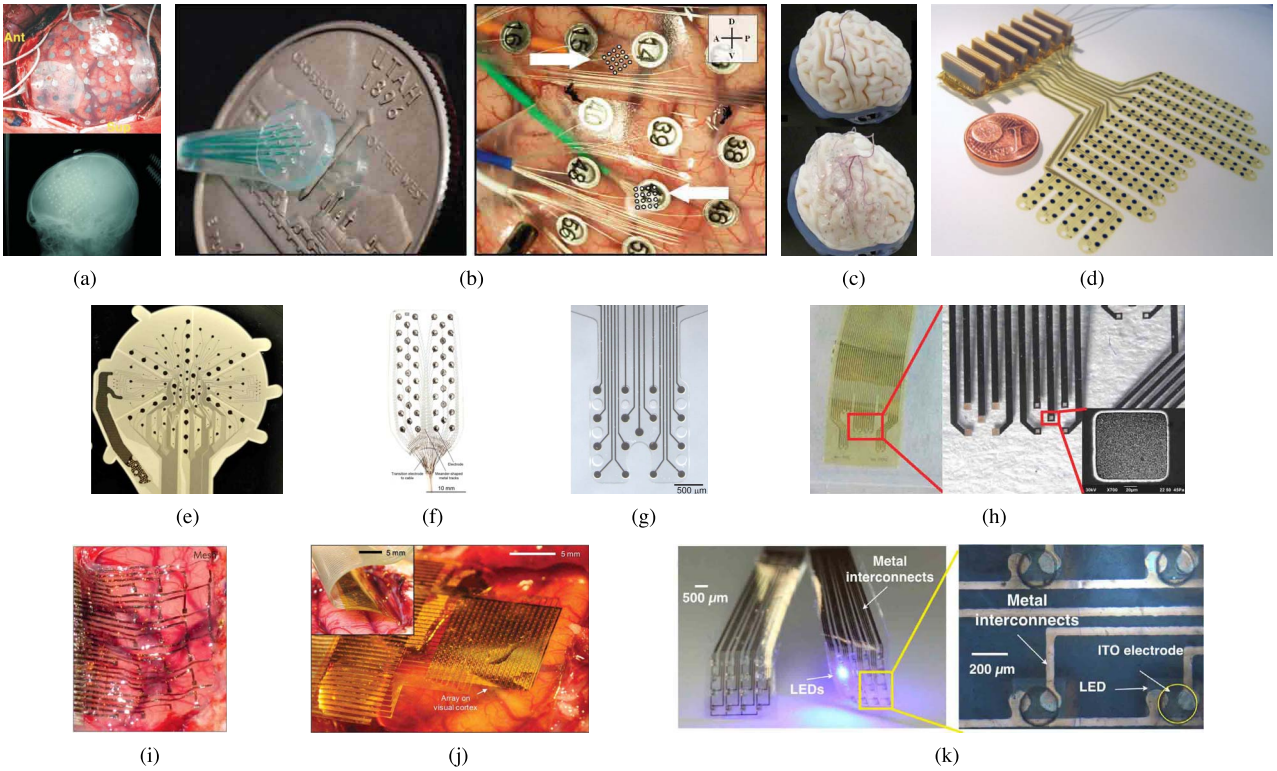

Fig. 4. ***Conventional and state-of-the-art ECoG electrode arrays. (a) Example of a conventional electrode array placed on the subdural cortex (top) with post-operative radiograph showing electrode array placement (bottom). The pitch and diameter of electrodes are 1 cm and 2 mm, respectively [20]. (b) μECoG electrode array placed along with a conventional ECoG electrode array [21], [22]. (c) Patient-specific electrode array for sulcal and gyral placement [23]. (d) Flexible 252-channel ECoG electrode array on a thin polyimide foil substrate [24]. (e) μECoG electrode array with 124 circular electrodes with three different diameters [25]. (f) Parylene-coated metal tracks and electrodes within a silicone rubber substrate [26]. (g) A transparent μECoG electrode array with platinum electrodes on a Parylene C substrate [27]. (h) An electrode array with poly (3, 4-ethylenedioxythiophene) (PDOT) and PEDOT-carbon nanotube (CNT) composite coatings for lower electrode interface impedance [28]. (i) A flexible electrode array on a bioresorbable substrates of silk fibroin [29]. (j) Flexible active electrode array with two integrated transistors on each pixel for ECoG signal buffering and column multiplexing for high channel count [30]. (k) Flexible ECoG array with embedded light-emitting diodes for optogenetics-based stimulation [31].***

B. Electrode Interfaces for ECoG

Electrodes, which couple ECoG signals from the brain into the analog front-end (AFE) amplifiers, are the first interface to ECoG systems. Thus, their properties, including materials, geometries, and placement are of crucial importance in building entire acquisition and actuation systems [32].

Given the distance between the scalp and individual neuronal current sources and sinks, EEG recording is unsuitable for detecting small local field potentials as shown in Fig. 2(a). Electrical dipole signals travel a minimum distance of 1 cm between the outer surface of the cerebral cortex to the scalp, including layers of cerebrospinal fluid, meninges, bone and skin, all with varying electrical properties. Through this path the effect of a small-localized dipole source is not only greatly attenuated but also spatially averaged among a myriad of neighbors, resulting in practical and theoretical limits to the spatiotemporal resolution of EEG [33]. As implied in (1), centimeter-sized electrode arrays with centimeter spacings in conventional ECoG recordings are better than EEG, but have limitations in resolving current sources of neural activity of size smaller than the electrode pitch. A conventional clinical ECoG array with electrodes at the centimeter scale is depicted in Fig. 4(a).

A miniaturized surface electrode array in direct contact with the cerebral cortex can resolve the activity of smaller source populations down to millimeter or even submillimeter resolution as shown in Fig. 4(b)–(k). Furthermore, site-specific purposeful electrical stimulation is only possible at μECoG scale. Improvements in the quality and applications of ECoG data have resulted from technological developments at the interface: microfabrication of electrode and substrate materials and interconnect. Simply miniaturizing existing electrode array is not typically sufficient: for example, miniaturized electrodes

Table 1 Design Factors and Tradeoffs in Integrated ECoG Interfaces

Design Factors	Trade-Offs and Inter-Relations	Typical Range (ECoG)	Examples	Comments
Input Referred Noise	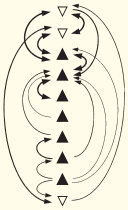	1–5 μV_{rms}	[45, 51, 56]	Dominated by electrode interface and front-end amplifier
Power Consumption		0.1–10 μW	[46, 57, 54]	Lowered by biasing, or duty cycling/multiplexing above Nyquist rate
Bandwidth		0.1–500 Hz	[44, 66, 73]	ECoG signal bands
Dynamic Range (DR)		40–120 dB	[55, 64, 65]	Variable gain compounds signal-to-noise ratio for extended DR
Variable Gain		1–1,000 V/V	[42, 46, 54]	Typically digitally selectable with auto-ranging capability
Power Supply Rejection Ratio (PSRR)		40–80 dB	[42, 43, 73]	Frequency dependent, limiting switching regulator frequency
Common-Mode Rejection Ratio (CMRR)		60–120 dB	[42, 43, 45]	Mains interference rejection
Input Impedance		100 MΩ–10 TΩ	[48, 49, 78]	Resistive/capacitive; depending on the contact type and application
DC and Low-Frequency Rejection		0.1–1 Hz	[43, 47, 49]	AC coupling; with CDS or chopping for $1/f$ noise and offset reduction
Area / Size		0.1–10 cm^2	[48, 66, 94]	Dominated by electrodes and battery; minimizing off-chip components

▲: factors to be maximized; ▽: factors to be minimized

in < 1 mm pitch arrays have very high impedance, which results in poor signal quality, and reduced charge transfer capacity, which typically reduces stimulation efficiency. Such limitations have been addressed by micropatterning increased surface area, and carbon nanotube [34] or conductive polymer coatings [Fig. 4(h)] [28]. Flexible substrates have also reduced the effective distance between source and electrodes through tight, conformal geometries [24], [26]. Aside from creating ultraflexible thin materials, dissolvable substrates leave behind a mesh of thin unobtrusive wires and electrodes with a superior curved conformation and biocompatibility as shown in Fig. 4(i) [29], [35].

Even with advances in flexible electrode arrays, the number of channels in practical systems is still limited to approximately 100 because of the high density of interconnections between electrode arrays and corresponding acquisition systems. Active electrodes are an emerging approach to maximize number of electrode channels while maintaining a small number of wired connections to the electrode array. Advanced fabrication techniques can produce arrays of electrodes with direct integration of transistors on the flexible substrate as shown in Fig. 4(j) [30] This approach can be supplemented with additional *in situ* devices capable of multiplexing several hundreds of recording channels, thereby reducing the required number of wires and interconnections. Another emergent approach combining active recording electrodes and new polymeric materials has led to the development of organic electrochemical transistors in ECoG arrays [36]. However, one limitation of current active arrays is that the same electrode cannot be used for stimulation. Recently, transparent electrode arrays with integrated light path for simultaneous ECoG recording and optogenetic stimulation have been demonstrated as shown in Fig. 4(k) [31]. The active development of novel electrode interfaces has not only improved conventional ECoG recording, but also generated new applications and therapeutic opportunities.

C. Integrated Circuit Interfaces for Data Acquisition

Neural data acquisition with a high spatial resolution poses several challenges in the design of application-specific integrated circuits (ASICs) used to perform data acquisition. Higher channel density in ECoG arrays typically results in smaller electrode size, and if the area overhead of the ASIC should be kept small, as is desired in most applications, then the area dedicated to amplify and digitize each channel should also reduce. Unfortunately, area trades off with several important parameters. For example, a more dense array of AFE amplifiers dissipates more power and generates more heat for each channel, and thus power dedicated to each front-end channel must reduce to meet thermal regulatory limits. Power then trades off with noise, causing signal fidelity issues. The area/volume constraint of front-ends typically also precludes the use of external components such as inductors or capacitors. As a result, alternating current (ac) coupling capacitors employed to reject direct current (dc) or slowly time-varying electrode offsets are not typically employed, so other techniques are instead necessary. Small electrodes also have higher impedance, requiring even higher AFE input impedance to avoid signal attenuation. In addition, high power supply rejection ratio (PSRR) is required because miniaturized implants typically condition dc power from an external ac source, and further may not be able to accommodate large power decoupling capacitors. Higher channel counts also require higher communication throughput, increasing the power consumption of communication. All these requirements are interrelated and trade off with each other in many ways, as indicated in Table 1 [32], [37], [38].

The noise-current tradeoff in instrumentation amplifiers (IAs) is well represented by the noise efficiency factor (NEF), which is expressed as

$$\mathrm{NEF} = V_{\mathrm{rms,in}}\sqrt{\frac{2I_{\mathrm{tot}}}{\pi V_t \cdot 4kT \cdot BW}} \tag{3}$$

where $V_{\mathrm{rms,in}}$ is the total input-referred noise, I_{tot} the total current drain, V_t the thermal voltage, and BW the 3-dB bandwidth of the system [39]. To minimize noise with a given current consumption or minimize current consumption with a upper-bound noise limit, various

design techniques have been proposed and demonstrated to address this challenges [40]–[59]. Such techniques to minimize NEF include 1) utilizing the weak inversion region of CMOS operation to maximize transconductance efficiency [37], [40], [60], [61]; 2) chopper stabilization techniques to reduce $1/f$ noise and other low-frequency noise [41], [43], [45], [47], [48], [62], [63]; 3) dynamic range manipulation to reduce power supply voltages [54], [55] using spectrum-equalizing AFE [64], [65]; and 4) using current-reusing nMOS and pMOS input pairs to maximize transconductance and achieve an NEF below two [54], [56]–[59] (Fig. 5).

Challenges in meeting the other specifications listed in Table 1 have also been addressed using various circuit techniques. For example, several dc-coupling IAs have been demonstrated in order to avoid external ac-coupling capacitors at the input of the AFE [42], [43]. In these designs, electrode offsets are canceled by feedback currents via a dc-servo loop [42], [43] or by capacitive feedback [66].

Integration of higher channel count on a single chip has been pursued, as well. Thus far, chips with approximately 100–300 data acquisition channels have been reported [54], [67]–[70]. One of the strategies to reduce area and power consumption in order to maximize channel density is the use of scaled processes such as 65-nm complementary metal–oxide–semiconductor (CMOS) [66], achieving 64 channels with a silicon area of 0.025 mm^2 per channel. For higher density, in some designs, a SAR ADC is shared by about 8–16 AFEs using a time multiplexer [54]. In doing so, power-efficient multiplexers [71] and time-interleaving sample-and-hold circuits in SAR ADCs have been demonstrated. Alternatively, a dedicated ADC per AFE channel has been also pursued due to its ease of integration with a larger number of channels [44], [66].

D. Integrated Circuit Interfaces for Stimulation

Historically, electrical stimulation on the cortical surface was pioneered by Penfield [72] as intraoperative planning for epileptic patients, demonstrating the localized function of different regions of the cortex [73]. Since then, functional neural stimulation has been extensively investigated and developed during the past decades, making great progress for various clinical applications such as deep brain stimulation, cochlear implants, cardiac pacemakers, bladder control implants, and retinal prostheses. Given that many epilepsy patients already require implantation of ECoG monitoring instrumentation, there is a great opportunity for closed-loop electrical control of seizure activity at much higher resolution and precision than transcranial electric [74] and transcranial magnetic stimulation [75], [76]. These embedded stimulators would not require any additional invasive risks, and could potentially prevent more drastic treatments such as partial removal of the cortex. An

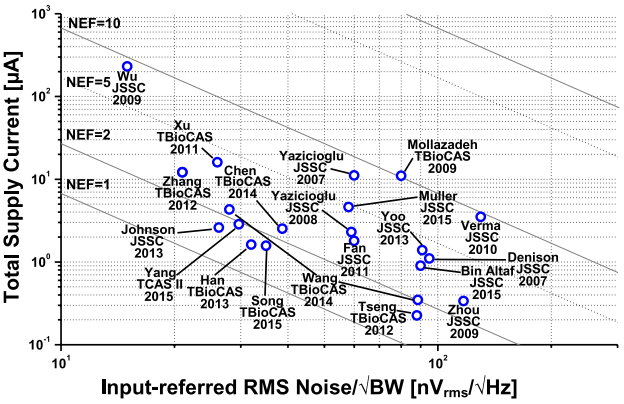

Fig. 5. ***Noise efficiency factors of state-of-the-art instrumentation amplifiers for biopotential recording applications.***

implantable recording and stimulation system can contain a digital signal processor capable of deciding when to stimulate [77]. Other applications of cortical stimulation include closed-loop brain computer interfaces (BCI) which aim to generate functional maps of the brain [78], restore somatosensory feedback [76], restore motor control to tetraplegics [79], aid stroke survivors [80], [81], restore vision [82], reduce pain [73], or even change emotional state [83].

Pushing the form factor and channel density of the neural interface systems to the limit requires addressing several challenges in ASICs for stimulation. Smaller form factor and higher channel density require smaller electrode size, which limits charge transfer capacity for effective stimulation. Hence, higher voltage rails of more than ± 10 V and/or high-voltage processes are required typically [84]–[86], in turn this results in higher power consumption, larger silicon area, and system complexity to generate and handle high-voltage signals. Instead of maintaining a constant high-voltage power supply, some designs save power by generating a large power rail only when actively stimulating [77], [87], [88].

For further power savings, adiabatic stimulation has been also actively investigated. Adiabatic stimulators generate ramping power rails that closely follow the voltages at the stimulation electrode, minimizing unnecessary voltage drops across the current source employed for conventional constant-current stimulation. Various designs have been implemented with external capacitors [89], external inductors [90], and charge pumps [87]. Still, there is much room for improvement in the implementation of adiabatic stimulators in fully integrated, miniaturized implantable ICs.

It is generally desired to minimize the area occupied per stimulation channel for high-density integration. To date, integration of 100–1600 channels has been

achieved [84]–[86], [91]–[93]. In order to integrate such high channel counts, programmability of waveform parameters, individual connectivity to each channel, and/or charge balancing need to be compromised to some extent. For example, groups of 4–8 electrodes in [91], [93]–[95] can share a single digital-to-analog converter for optimized, high density integration.

Safety is of the utmost importance in chronic neural interfaces, so charge balancing is imperative [96]. Residual dc results in tissue damage, production of toxic byproducts, and electrode degradation [96]. However, it is quite challenging to assure charge balance for each channel in high-channel neural interface systems. One of the most straightforward strategies is to employ serial dc-blocking capacitors, inherently forcing the net dc to be zero all the time. This method has been employed for neural stimulation applications [97]–[99] due to its intrinsic safety when area permits. However, the required blocking capacitance is often prohibitively large for on-chip integration, and is thus inadequate for high-density and/or miniaturized implants. Instead of external capacitors, capacitive electrodes made with high-k dielectric coatings have been investigated for safe neural interfaces [88], [100], [101]. Several other techniques for better charge balancing have been demonstrated: 1) shorting electrodes to ground [102]; and 2) utilizing a discharging resistor [94], active current balancing by feedback control [103], [104], generating additional balancing current pulses by monitoring electrode voltages [105], and embedded DAC calibration [93], [106].

E. Integrated Electrocortical Online Data Processing

The integration of signal processing with neurophysiological sensing and actuation enables real-time online control strategies toward realizing adaptive, autonomous closed-loop systems for remediation of neurological disorders [107], [108]. Online signal processing of ECoG data has tremendous potential to improve patient outcomes in diseases currently lacking therapy or requiring resection of otherwise healthy neural tissue such as intractable epilepsy. As one of the treatments for epilepsy, functional neurostimulation in response to detected seizures has been proved effective in reduction of seizures [109], [110]. For real-time closed-loop therapeutics, online automated seizure prediction and/or detection based on ECoG or EEG recordings of epileptic patients is imperative [111]–[114], and their on-chip implementation has been actively investigated and demonstrated utilizing extraction and classification of various signal features such as power spectral densities and wavelet coefficients [47], [77], [115]–[118].

In addition, ECoG has proven a powerful modality for BCI applications owing to richer features present in the higher resolution ECoG signals compared to surface EEG, which can be harnessed to more precisely infer sensory recognition, cognition, and motor function. Since ECoG-based BCI systems widely utilize spectral power density for their inputs [119], frequency band power extraction techniques have been implemented immediately following AFEs avoiding digitization and RF data transmission of whole ECoG raw signals [120], [121].

Such on-chip real-time ECoG data processing offers two distinct advantages over offline as well as online off-chip processing. First, constrains on data bandwidth and power consumption on the implant can be largely relieved. In many implementations, raw recorded data are wirelessly streamed out and delivered to either a unit worn on the top of the head, or directly to a local base station such as a smartphone. The power of such approaches is typically proportional to the communication distance. Thus, the overall power consumption of designs that stream over long distances can be dominated by the power of communication circuits [47]. In order to reduce system-level power consumption, several on-chip data processing techniques have been applied for EEG- and ECoG-based BCI systems and epileptic seizure detection. By doing so, power consumption of RF data transmission can be drastically reduced [47]. Second, local processing may alleviate stringent latency and buffer memory requirements in the uplink transmission of data for external processing, especially where multiple implants are time-multiplexed between a common base station.

III. SYSTEM CONSIDERATIONS

A. Powering

Major challenges in implantable medical devices (IMDs) for high-density brain activity monitoring are fundamentally posed by their target location. Some of these IMDs can be wholly placed on the cortex within a very limited geometry as shown in Fig. 2(b) In other cases, only the electrode array is placed on the cortex while the other components can be located in the empty space created by a craniotomy [122], or under the scalp with lead wires connected [123], [124]. Regardless of placement, this constrained environment poses a difficult power challenge.

There are three primary methods for powering an implanted device: employing a battery, harvesting energy from the environment, and delivering power transcutaneously via a wireless power transmitter [125], [126]. A natural first choice would be a battery, as they have been extensively used in other implantable applications such as pacemakers. While it makes sense to use a battery in a pacing application, where the power of the load circuit is small (microwatts) and a large physical volume is available such that the battery can last ten years or more, the power consumption in high-density neural recording and stimulation applications is typically much larger (milliwatts), and the

physical volume available for a large battery is small, combining to dramatically reducing operational lifetime prior to necessary surgical reimplantation. The medical risks of regular brain surgery and recovery, just to replace a battery, are unacceptable to most patients, and thus batteries are typically only employed in high-density neural applications as temporary energy storage in systems with a different power source: either energy scavenging or wireless power transfer.

Harvesting energy from ambient sources in the local environment has been a potentially attracting powering option since at least the 1970s during the development of cochlear implants. Many scavenging methods continue to be actively developed: 1) solar cells; 2) biofuel cells; 3) thermoelectric generators; 4) piezoelectric generators; 5) ambient RF, etc. While such approaches are theoretically attractive, the limited volume available near the brain, coupled with the stochastic nature of many energy harvesting sources, results in power that is too small and too variable to reliably operate multichannel neural technologies.

The most popular means to power an implanted device with higher power than single-channel pacing applications is to wirelessly delivery power via a transcutaneous link. Power can be delivered transcutaneously using one of three primary mechanisms: 1) optics (typically near infrared light); 2) acoustics (typically at ultrasound frequencies); and 3) electromagnetics (either near-, mid-, or far-field waves). Each method can deliver from 10 μW up to the megawatt range of power. However, the total deliverable power highly depends on the geometry and makeup of the receiving transducer, along with the implant depth and orientation.

Optical powering through transmission of infrared light has a very short penetration depth of a few millimeters, limiting its utility to subcutaneous and very shallow implant applications [130]–[132]. Ultrasound, on the other hand, can penetrate much deeper into tissue, potentially powering implants located on the cortical surface. In fact, it has been demonstrated that ultrasound can more efficiently power millimeter-scale devices implanted deep into soft tissues than electromagnetic approaches [133]. However, it has also been shown that ultrasonic energy does not efficiently penetrate bone, limiting opportunities to directly power cortical implants from outside the skull. To overcome this, researchers have proposed two-tiered systems, where electromagnetic energy is coupled through the skull, then converted to acoustic energy via an intermediate transducer system, and finally delivered to the miniaturized implant through soft tissue [134]. However, in addition to nontrivial packaging and transducer design challenges, this is likely only a reasonable approach when the implant to be powered is either very deep, or very small (submillimeter scale). For these reasons, ultrasonic power delivery is not typically considered for ECoG systems.

The most popular transcutaneous power delivery approach utilizes electromagnetics. For devices implanted to a depth of a few centimeters, and that are on the order of millimeter-to-centimeter in diameter, near- or mid-field electromagnetic power transfer is generally considered to be the most efficient and practical method to power such devices. Near-field power transfer, which operates at frequencies up to approximately 100 MHz for typical implants, has been extensively used for cochlear implants [135], retinal prostheses [86], [93], and various research IMD systems [122], [136]–[139], and has been investigated and characterized to maximize its usage and power transfer efficiency for implants [140]–[145].

Most conventional designs operate in the near-field between 1 and 20 MHz, since it is well known that conductivity (and hence losses) in tissue increase at higher frequencies, as shown in Fig. 6. Operating at higher frequencies, it was previously argued, would encounter higher losses and thus be less efficient. In addition, governmental regulatory agencies limit the amount of power that can be dissipated in tissue for safety reasons—the U.S. Federal Communications Commission (FCC) sets a specific absorption rate (SAR) of less than 1.6 W/kg, for example. For these reasons, conventional transcutaneous power transfer links operate in the low-megahertz range, often at the 6.78- and 13.56-MHz ISM bands [125], [144], [145].

However, it is also well known that the quality factor and radiation resistance of electrically small coil antennas increases with increasing frequency. Thus, miniaturized implants, which have electrically small coils for wireless power reception, tend to prefer to operate at higher frequencies, at least in air. In biological tissues, the tradeoff between coil design and tissue losses results in an optimal frequency for wireless power transmission where efficiency is maximized. For example, the inductance of coils located on miniaturized, millimeter-scale implants ranges from 10 to 100 nH [66], [88], [146], [147]. To compensate for reduced magnetic flux through the miniaturized receiving coil, the carrier frequency for wireless power transfer should be increased, often into the hundreds of megahertz to single-digit gigahertz range [66], [146]–[149]. These prior studies have demonstrated that it is possible to efficiently deliver milliwatts of power to small, implanted devices under regulatory limits, and thus electromagnetic approaches are the primary means to deliver power to implanted ECoG devices.

B. Wireless Data Communication

Implanted ECoG monitoring devices need to convey the acquired data to the external world through wireless communication. The information received by the external base station can be monitored, processed, and used by users and care takers for health monitoring, treatments, or scientific research. For ECoG monitoring

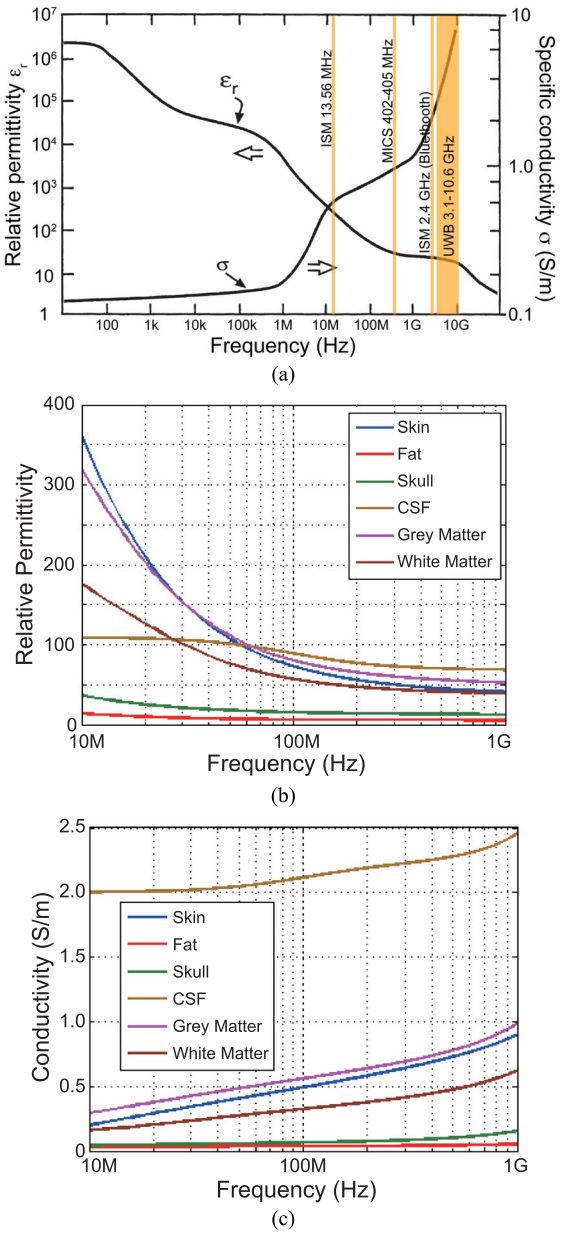

Fig. 6. ***(a) Relative permittivity and specific conductivity over frequency range from 10 to 100 GHz with most popular frequency communication bands for ECoG implants [127], [128]. (b) Relative permittivity and (c) specific conductivity of various kinds of tissues including skin, fat, skull, CSF, gray and white matter [129].***

implants, data transmission from the implant to the external device, known as uplink or backward telemetry, requires much higher data rate and is subject to more stringent power consumption constraints than data transmission from the external device to the implant, known as downlink or forward telemetry, because the available power and geometric volume are much smaller on the implanted side than the external side. This power constraint on backward data transmission is more exacerbated as the number of channels increases, as higher data rates are required in a typically more compact area, leading to severe power density challenges.

Backward data communications typically employ electromagnetics operating either in the far- or near-field. Far-field communication uses electromagnetic radiation to transmit data over a distance much longer than the size of the actual device. Hence, the implant can send data to an external base station located up to a few meters, such as mobile phone. Far-field up-conversion transmitters are currently the most well-established communication technology. Due to the wide availability of far-field radio products and a myriad of different infrastructures (e.g., Bluetooth Low Energy, WiFi, etc.), far-field radios can be quickly adopted for robust operation [122]. However, even state-of-the-art low-power radios consume > 1 nJ/b [125], [164], which is order-of-magnitude larger than what typical ECoG recording IMDs require.

As an alternative far-field transmission method, impulse radio ultrawideband (IR-UWB) transmission has emerged recently due to its low power consumption in the range of a few tens of picojoule per bit (pJ/b) [165]–[167]. Avoiding generation of a carrier with an accurate frequency, noncoherent IR-UWB transmitters generates short pulses with ON–OFF keying (OOK) or pulse position modulation (PPM). Due to its high and wide frequency range (3.1–10 GHz), data rates of more than 10 Mb/s with tens of picojoules per bit have been reported. [168] In addition, antennas for this type of transmission do not need to be large. However, there are a couple of critical reasons against their usage for IMDs [125]. Foremost, their peak transmission power is large due to the inherently duty-cycled nature of IR-UWB transmitters. Thus, while the average power may be low, a large high-quality power supply with a large battery of capacitor is required to supply large peak currents, which may be prohibitively large for many ECoG applications. Moreover, since IR-UWB operates at very high frequency over 3 GHz, tissue absorption rate is higher.

In contrast to far-field communication methods, near-field radios operate over short distances, typically within one wavelength of the carrier frequency, and are thus suitable for use when an external device is located directly on the head. In fact, since this configuration is naturally present in wirelessly powered devices, near-field communication can easily be implemented along with this wireless powering. One of the most popular data communication methods that can be implemented along with forward power delivery is the backscattering method [169]–[173]. This method modulates the load conditions of forward powering signals, and reflecting this energy back to the interrogator. Since only a single switch needs to be driven, the power consumed on the

implant side is minimal, as carrier generation and active driving of an antenna are not required. Since, with this technology, a few picojoules per bit to tens of picojoules per bit can be achieved [173], it has been widely adopted by various IMDs [66], [86], [174]–[178]. However, external data reception in backscattering systems can be challenging in some cases because of the large power difference between the large power carrier signal and the weak backscattered signal.

Forward telemetry for neural recording IMDs is typically used for sending configuration bits to the implant, requiring a relatively low data rate typically much less than 100 kb/s. Hence, amplitude shift keying (ASK) has been widely employed in such IMDs [88], [179], [180], modulating the power carrier signals. For IMDs with stimulation capability, forward telemetry for closed-loop operation is typically time-multiplexed with backward telemetry.

C. Hermetic Encapsulation

Implanted devices containing silicon ICs need packaging in a protective enclosure to mitigate corrosion and other contamination by surrounding electrolyte in the body [181], [182]. Thus far, titanium-, glass- or ceramic-based enclosures have been the primary means for hermetic sealing in long-term implants, since these hard materials have been shown to be biocompatible and impermeable to water [181]. Even though such hard enclosures are used in the majority of long-term implants [6], [111], [122], [150]–[155], [159], [183], their very large volume and weight, typically much larger than the ICs and supporting components they contain, prohibits their use in high-dimensional neural interfaces heavily constrained by anatomical space such as retinal prostheses [184] and μECoG arrays [30]. In addition, hard packaging requires intricate methods for hermetic sealing of feedthroughs to polymer insulated extensions of the implant such as electrode array cabling, limiting the density of electrode channels due to feedthrough channel spacing requirements.

To overcome these challenges, conformal coating of integrated electronics with polymers such as polyimide, silicone, and parylene-C have been investigated as alternatives. They are superior over metal, glass, and ceramic hard seals in miniaturization, flexibility, and compatibility with the semiconductor process [185]. However, polymers are susceptible to degradation and are not long-term impermeable to body fluids. While polymer encapsulation has been used for relatively simple and short-term (less than 1–2 years) implants, substantial improvements are needed for viable solutions to long-term hermetic encapsulation [182], [186]. Recent next-generation advances in miniaturized hermetic sealing of silicon integrated circuits, such as multilayer multimaterial coating [187], and encapsulation using liquid crystal polymers (LCPs) [185], are promising developments toward highly miniaturized implantable electronics for chronic clinical use. Furthermore, recent advances in dissolvable flexible electronics [188], [189] offer alternatives to hermetic encapsulation for acute applications without the need for post-use surgical extraction.

IV. STATE-OF-THE-ART ECoG INTERFACE SYSTEMS

Various types of implantable devices for ECoG interfaces have been developed for clinical use and neuroscience research. Their target applications include treatment of neurological disorders and ECoG-based BCIs. Fig. 7 illustrates several state-of-the-art ECoG interface systems for clinical and research applications.

On the clinical side, implantable devices shown in Fig. 7(a)–(c) have been developed mostly for use in closed-loop treatment of intractable epilepsy as an alternative to tissue resection. These devices monitor ECoG signals and deliver stimulation to the seizure foci in response to epileptic seizure detection. The NeuroPace RNS System, shown in Fig. 7(a), is the first such system to receive FDA approval for closed-loop treatment in epilepsy patients, proven effective to reduce the frequency of partial-onset seizures in human clinical trials [191], [192].

However, clinically proven devices are severely limited in the number of ECoG channels, typically less than ten, and rely on batteries, limiting implantation life time up to a few years. In addition, their physical size is too large to be implanted near the brain, so the main parts of these systems are implanted under the chest with a wired connection to the brain. Further developments in ECoG technology have striven to conquer these challenges: increasing number of channels, wireless powering, and miniaturization.

One such device is the Wireless Implantable Multichannel Acquisition system for Generic Interface with NEurons (WIMAGINE), which features up to 64 channels, targeting long-term ECoG recording fully implanted in human patients [122] as shown in Fig. 7(d). This active IMD (AIMD) is fully covered by a 50-mm-diameter hermetic housing made of silicone-coated titanium with a silicone-platinum electrode array on the bottom side. Its silicone over-molding is extended to include two antennas for RF communication and wireless power transfer. The housing fits inside of a 50-mm craniotomy, and its upper surface is just below the skin, with the implant replacing the previously existing bone. Two 32-channel ECoG recording ASICs [193] are implemented for ECoG recording, and commercial off-the-shelf components are employed for data processing, communication, power management, etc., leading to relatively high power consumption—75 mW for 32 channels. Its operation and

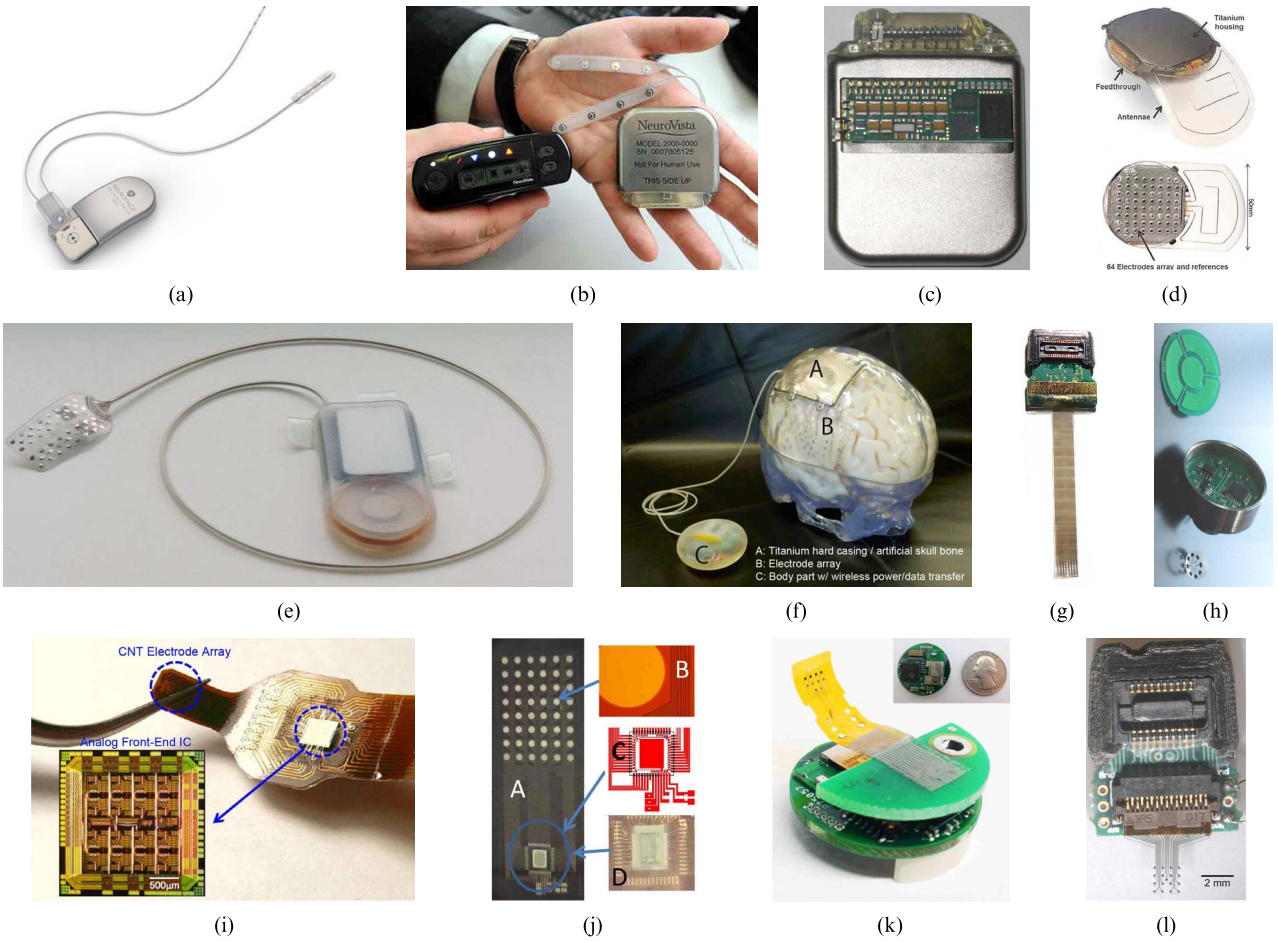

Fig. 7. ***State-of-the-art ECoG interfacing systems. (a) NeuroPace RNS system [150], [151]. (b) NeuroVista seizure advisory system [111], [152], [153]. (c) The neural interface (NI) system of Medtronic [154], [155]. (d) The Wireless Implantable Multi-channel Acquisition system for Generic Interface with NEurons (WIMAGINE) [122]. (e) BrainCon system for a general-purpose medical BCI [156]–[158]. (f) The Wireless Human ECoG-based Real-time BMI System (W-HERBS) [6], [159]. (g) μECoG recording system of Cortera Neurotechnologies, Inc. [66], [160]. (h) A ECoG recording system with bidirectional capacitive data Telemetry [161]. (i) An ECoG recording system with a carbon nanotube microelectrode array and a corresponding IC [34]. (j) A wireless ECoG interface system with a 64-channel ECoG recording application-specific integrated circuit (ASIC) [162]. (k) An 8-channel low-cost wireless neural signal acquisition system made with off-the-shelf components [163]. (l) μECoG recording system with an electrode array fabricated on a transparent polymer for optogenetics-based stimulation [27].***

biocompatibility has been evaluated *in vivo* in nonhuman primates.

Another example is the BrainCon system with 16-channel ECoG recording and 8-channel stimulation designed for chronic implanted use in closed-loop human BCI [158]. Shown in Fig. 7(e), this device consists of an ECoG electrode array and an electronic package with a magnet, an inductive coil, and electronic components for data acquisition, stimulation, and communication. Targeted for long-term recording and cortical stimulation in human patients, it is enclosed in a hermetic package with medical grade silicone rubber [156], [157], and was validated *in vivo* for more than ten months [158].

Further miniaturization and advances in functionality have been pursued through integration of circuits for ECoG recording, wireless powering, and wireless communication as shown in Fig. 7(f)–(j). In addition, low-cost ECoG interfaces shown in Fig. 7(k) for acute animal research have been developed [163], as have ECoG interfaces with transparent electrode arrays for compatibility with optogenetic stimulation shown in Fig. 7(l) [27].

Each of these devices offers substantial advances in wireless and integrated ECoG technology with improved functionality and increased density and channel counts. Yet, most rely on substantial cabling in connecting to the array of electrodes, or at least a wired connection to a distal ground as reference.

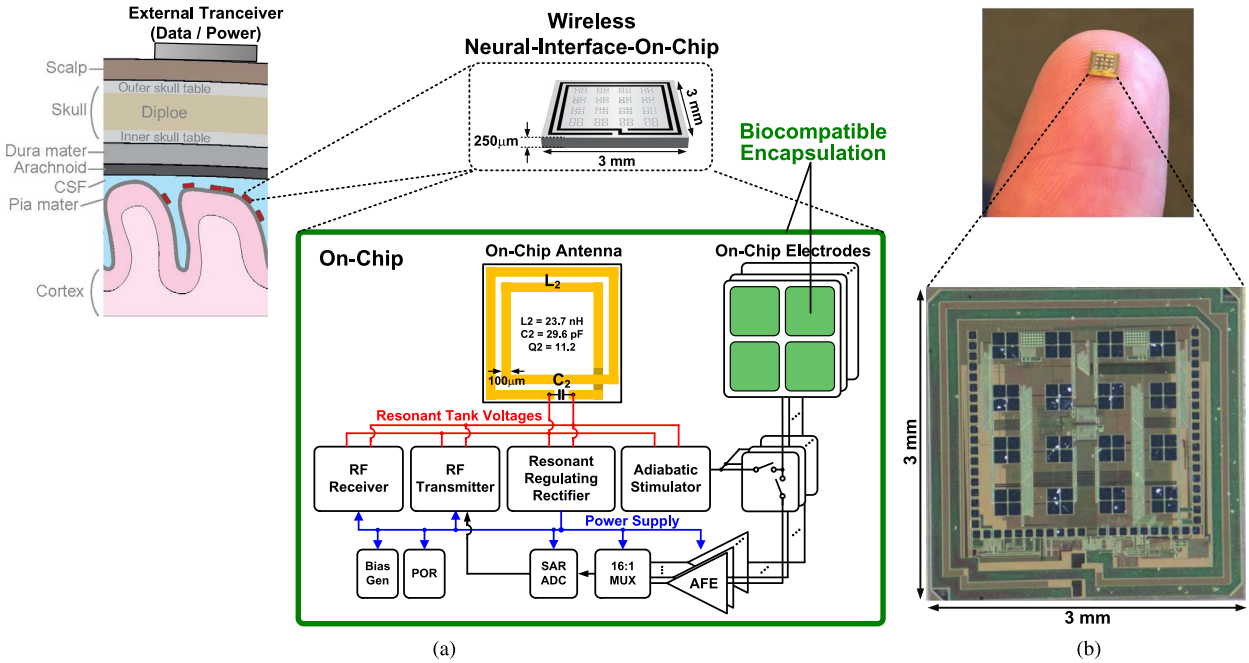

Fig. 8. ***Encapsulated neural interfacing acquisition chip (ENIAC) [88], [190]. (a) System diagram showing the fully integrated functionality of the ENIAC comprising on-chip antenna, electrodes, and all the circuitry for power management, communication, ECoG recording and stimulation. No external components are needed, and galvanic contact to surrounding tissue is completely eliminated in the fully encapsulated device. (b) Chip micrograph and dimensions of the prototype ENIAC.***

V. FULLY INTEGRATED MODULAR μECoG RECORDING AND STIMULATION

A. Encapsulated Neural Interfacing Acquisition Chip (ENIAC)

As highlighted above, most current state-of-the-art ECoG ASICs rely on external components, such as flexible substrates, electrode arrays, and antennas [27], [30], [66], [122], [156]–[158], [161], [162]. In doing so, integration of all the components into a complete system requires special fabrication processes, and, importantly, requires a large number of connections between the readout ASIC and the electrodes, which are very difficult to manage in a hermetic environment. Furthermore, electrodes typically make direct metal-electrolyte contact to the surrounding tissue, which can lead to generation of toxic byproducts during electrical stimulation. In addition, most systems do not support electrical stimulation, while those that do offer limited stimulation efficiency, or require large external components for efficient operation. Finally, the silicon area occupied by the ASIC limits the span and density of electrodes across the cortical surface. For ultrahigh channel count experiments, as needed for next-generation neuroscience and called for by several brain initiatives, such limitations must be overcome.

Instead of separating the electrodes and the ASIC, a promising approach that we present below is to integrate everything on a single encapsulated neural interfacing and acquisition chip (ENIAC), including electrodes, antennas for power and data telemetry, and all other circuits and components [88]. Thus, no external wires, substrates, batteries, or any other external components are required. Complete encapsulation of the ENIAC with a biocompatible material removes direct contact to tissue, including the electrodes for recording and stimulation. As such, the chip itself serves as a complete standalone neural interfacing system.

As shown in Fig. 8 the ENIAC is designed to be small enough $(3 \times 3 \times 0.25\ \text{mm}^3)$ to be placed among the folds and curves of the cortical surface [see Fig. 2(b)], and to be implanted through small skull fissures. Hence it offers greater coverage of the cortical surface while being much less obtrusive than other minimally invasive ECoG approaches, permitting even insertion without surgery. As seen in the block diagram in Fig. 8, the chip contains an LC resonant tank, electrodes, recording channels, stimulator, power management units, and bidirectional communication circuits.

Its first prototype, fabricated in a 180-μm CMOS silicon-on-insulator (SOI) process, is shown on the upper right side of Fig. 8. With two turns and 100-μm

thickness, the on-chip coil results in an inductance of 23.7 nH. The same single coil is shared for wireless power transfer and bidirectional RF communication. Sixteen electrodes, which can be individually configured as recording or stimulating channels, are integrated directly on the top metal layer of the chip. To enhance energy efficiency and remove the need for separate rectification and regulation stages, an integrated resonant regulating rectifier IR^3 [190] is implemented. In addition, an adiabatic stimulator generates constant-current stimulation pulses from the RF power input in an adiabatic manner, much more energy efficient than conventional stimulation from dc static power supplies.

B. Power and Communication

As highlighted in Section III-A, RF inductive powering is the most efficient means for power delivery at this implantation depth, and has been adopted in ENIAC. To model the inductive link through tissue, a detailed finite element method (FEM) model of the octagonal loop transmitter antenna and the $3 \times 3 - \text{mm}^2$ ENIAC shown in Fig. 9(a) was constructed in ANSYS HFSS, using tissue spectral permittivity and absorption properties as shown in Fig. 6(b) and (c). Optimal power transfer between the transmitter coil and ENIAC is reached at a resonance frequency of 190 MHz as shown in Fig. 9(b). At this frequency, substantially more than the required 2-mW power can be delivered under the specific absorption rate (SAR) limit (2 W/kg in IEEE std. 1528). Fig. 9(c) shows the maximum transmit power at the SAR limit, and corresponding maximum deliverable power at the implant, for varying distance of the air gap between the loop transmitter and the scalp. The optimal distance for maximum power delivery, trading between reduced SAR-limited transmit power at lower distance and increased path losses at higher distance [194], was found to be around 5 mm.

ENIAC minimizes power losses in the received power from the RF coil owing to an integrated resonant regulating rectifier (IR^3) architecture that combines power management stages of rectification, regulation, and dc conversion, eliminating typical losses due to inefficiencies at each stage when implemented separately. As illustrated in Fig. 10(a), IR^3 generates a constant power supply 0.8 V independent of fluctuation in the LC tank voltages. IR^3 operates by adapting both width and frequency of pulsed rectifier switching based on a feedback signal derived from V_{DD} [190].

Concurrently, the amplitude-shift-keying (ASK) demodulator tracks and amplifies the envelope of the LC tank voltages to decode transmitted configuration data as illustrated on the bottom of Fig. 10(a). The ASK communication is used to wirelessly configure the operation modes and parameters of the chip. To synchronize data reception, a 16-b predetermined identification code is used as prefix followed by serial peripheral interface (SPI) signals.

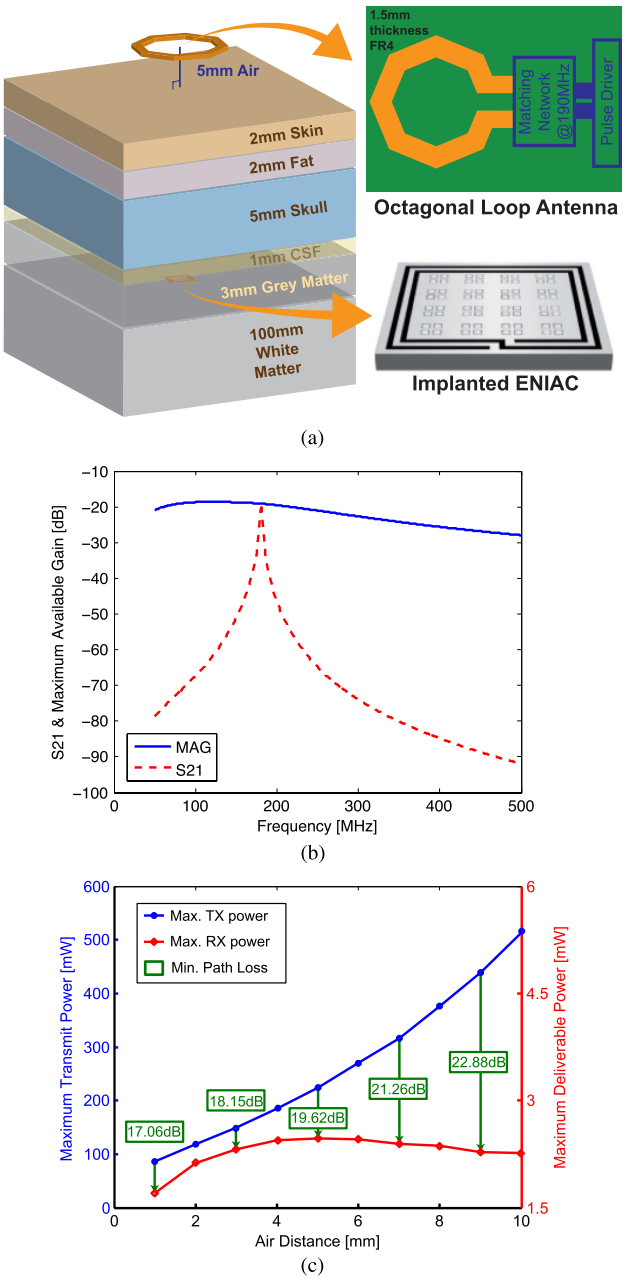

Fig. 9. ***(a) Three-dimensional finite element method (FEM) modeling of brain tissue layers between external transmitter and implanted ENIAC. (b) Simulated forward transmission coefficient S_{21} and maximum available gain (MAG) from the transmitter to the implanted ENIAC. The optimal frequency for wireless power transfer is around 190 MHz. (c) Maximum transmit power limited by specific absorption rate (SAR) and maximum receivable power at the implanted ENIAC, as a function of distance of air gap between the transmitter and the scalp, optimum around 5 mm. Green arrows denote minimum path losses at each air distance.***

Fig. 10(b) shows test setup and sample data for the IR^3 power delivery and the ASK data transmission. For these tests, a primary coil built on a printed-circuit board

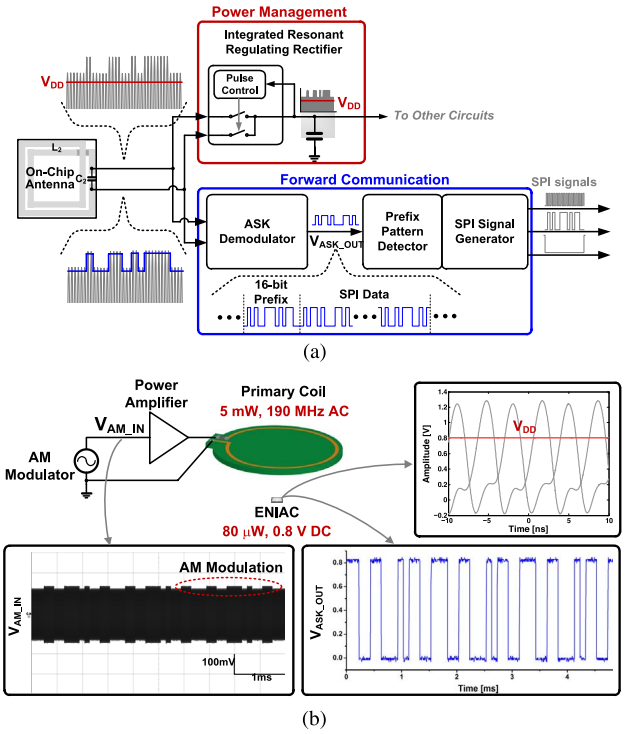

Fig. 10. *(a) System diagram of ENIAC power management and ASK forward communication, sharing the same single on-chip loop antenna. The integrated resonant regulating rectifier* (IR^3) *generates a stable 0.8-V dc output voltage directly from the 190-MHz RF coil voltage while the ASK demodulator decodes and amplifies the modulated signal. (b) Simplified test setup for wireless powering and communication along with measurement samples at the transmitter and the receiver.*

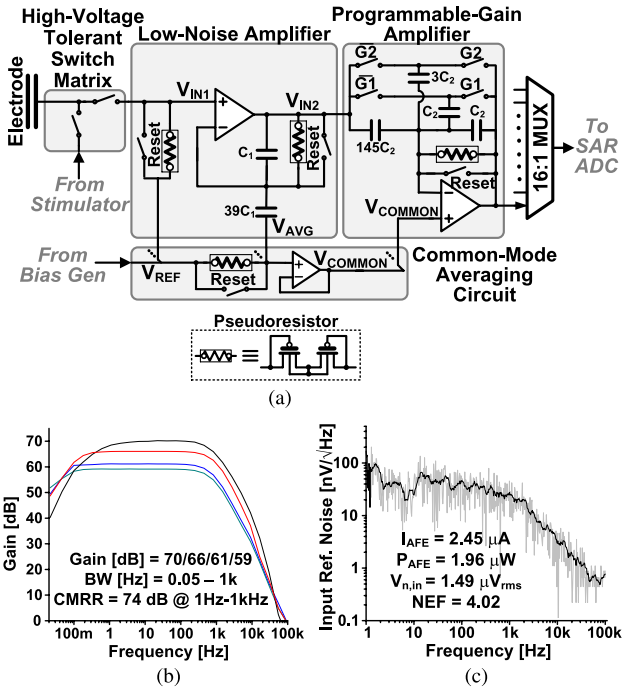

Fig. 11. *(a) Circuit diagram of the recording module of ENIAC with 16 AFE channels, 16:1 analog multiplexer (MUX), and successive approximation register (SAR) ADC. (b) Measured frequency and noise characteristics of one AFE channel.*

was placed 1 cm above the ENIAC. The top right panel in Fig. 10(b) shows the measured coil voltages simultaneously rectified and regulated by the IR^3 [190], [195] to produce the supply voltage $V_{DD} \approx 0.8$ V. The total transmitted power is about 5 mW, of which around 80 μW is received by the ENIAC. The bottom panel of Fig. 10(b) shows the AM modulated input on the primary side, and the demodulated ASK signal in the ENIAC.

C. Recording

The recording module integrates 16 AFEs, a 16:1 analog multiplexer (MUX), and an analog-to-digital converter (ADC) as shown in Fig. 11(a). Each of the 16 capacitively coupled electrodes is connected either to its local AFE channel, or to the global stimulator, multiplexed by a high-voltage tolerant switch matrix. The AFE amplifies the biopotential V_{IN1} from the capacitively coupled noncontact electrode with two amplification stages and a common-mode averaging circuit. The common-mode averaging circuit constructs a single reference signal V_{AVG} as the average of all V_{INi} electrode voltages through capacitive division. Similar to differential recording across a pair of adjacent electrodes (Section II-A1), the internal common-mode reference V_{AVG} allows single-ended recording over all 16 electrodes without the need for a distal external ground connection. A pMOS-based pseudoresistor [in the inset of Fig. 11(a)] is used to set the dc operating point at V_{REF} for the capacitive division to allow for very high ($T\Omega$-range) resistance in very small silicon area [40], [196].

The first low-noise amplifier stage has a noninverting configuration with a feedback capacitor C_1 and a common-mode coupling capacitor of $39 \cdot C_1$, which connects to the common-mode averaging node V_{AVG}, resulting in a differential voltage gain of 40 (V/V). V_{AVG} is buffered and used for common-mode rejection in the second AFE stage. The second AFE stage provides variable gain by manipulating the connections of two capacitors, connected either as input or as feedback capacitors [46], [54]. Output signals of the AFEs are multiplexed and buffered to the SAR ADC, which has time-interleaving sample-and-hold input DACs to ensure longer sampling time, leading to power saving in buffering the input DAC of the ADC.

Measurement results for the AFE, characterizing its frequency response and noise performance, are shown in Fig. 11(b) and (c). Variable 50–70-dB gain is supported,

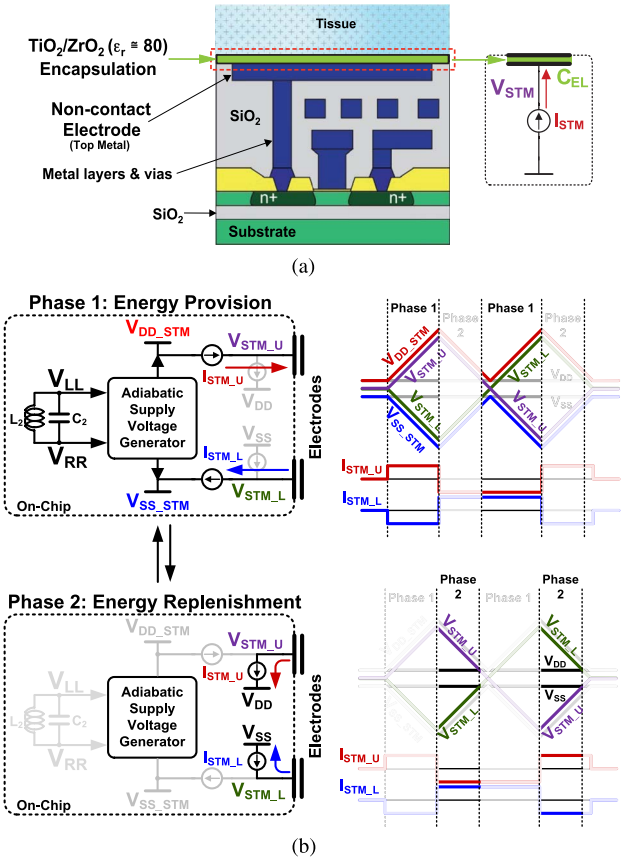

Fig. 12. ***(a) Simplified stackup of ENIAC showing an electrode coated with high-k materials for capacitive interface. (b) Principle of adiabatic stimulation with ENIAC. During the first phase, adiabatic voltage rails are generated directly from the LC tank for energy-efficient stimulation. During the second phase, the energy stored across the capacitive electrodes is replenished for further energy savings.***

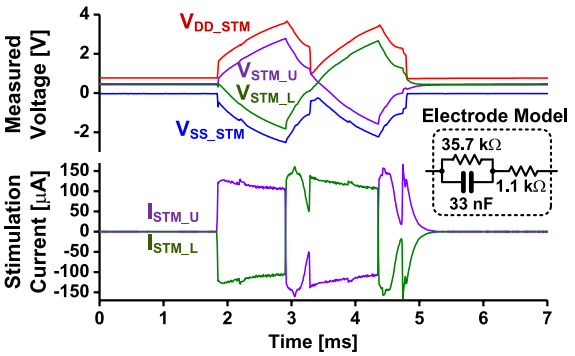

Fig. 13. ***Measured stimulation voltage and current waveforms with platinum model electrode.***

and the input-referred noise is 1.5 μV_{rms} at 2.45 μA supply current for a noise efficiency factor (NEF) of 4.

D. Stimulation

As illustrated in Fig. 12(a), ENIAC on-chip electrodes are implemented on top metal, as used for bond pads and on-chip inductors. The exposed electrodes allow for direct coating with a thin film of high-k materials such as TiO_2/ZrO_2 to achieve high capacitance for high charge delivery capacity. With 30-nm coating and $250 \times 250\ \mu m^2$ area, the coupling capacitance C_{EL} is about 1.5 nF, one order of magnitude smaller than that of a platinum electrode of same area. Total deliverable charge per phase Q_{ph} can be expressed as

$$Q_{\text{ph}} = I_{\text{STM}} \cdot T_{\text{ph}} = C_{\text{EL}} \cdot V_{\text{DD\_STM}} \tag{4}$$

where I_{STM} is the stimulation current, T_{ph} the time duration of the phase, and $V_{\text{DD\_STM}}$ the total voltage dynamic excursion. Relatively low capacitance C_{EL} can thus be compensated by an increased total voltage excursion $V_{\text{DD\_STM}}$ to deliver the required charge per stimulation phase. In order to achieve $Q_{\text{ph}} = 10$ nC per stimulation phase, needed for effective neural stimulation under typical electrophysiological conditions, a dynamic voltage rail with a total excursion of more than eight times the static supply voltage $V_{\text{DD}}(= 0.8\ \text{V})$ is required.

Conventionally, this can be implemented by generating the required high power supply voltages and supplying constant currents from fixed power rails. However, drawing currents in this manner incurs large energy penalties due to the large voltage drop across the current source.

Instead, a much better way to perform stimulation is to slowly ramp up the supply rails in an adiabatic fashion to minimize the voltage drop across the current source. Generation of the adiabatic voltage rails can be implemented in various ways. External capacitors [89] or an external inductor [90] can be employed. Alternatively, pulse width control in rectifier can be used [199]. However, all of these methods have output ranges within the LC tank swing voltages or V_{DD}. Recently, on-chip charge pumps are employed to generate a wide voltage excursion for adiabatic stimulation [87]. Because this approach utilizes the dc power supply as the input of charge pumps, series of power efficiency loss cannot be avoided in implantation settings. In addition, this method could generate discrete levels of power supplies only, so the energy losses due to the voltage drops across the current source were considerable.

In contrast, ENIAC implements an adiabatic stimulator that generates, at minimum energy losses, ramping voltage power rails with greater than eight times the voltage excursion of the LC tank, and with no need for any external components. Consistent with the observations in Section II-A2, differential adiabatic stimulation across a selected pair of electrodes is implemented, since

Table 2 Comparison of State-of-the-Art Wireless Integrated ECoG Recording and Stimulation Systems

Reference		[77]	[197]	[122], [193] WIMAGINE	[66], [198]	This Work ENIAC
Number of Channels		8[a]	64	32	64	16
Technology		0.18 μm	0.18 μm	0.35 μm	65 nm	0.18 μm SOI
Power Supply [V]		1.8	1.8	3.3	0.5	0.8
Total Power Consumption [mW]		2.8	5.4[b]	72.1	0.22	<0.1
IC Area [mm^2]		13.47	26.83[b]	86[b]	5.76	9
Total System Volume [mm^3]		N/A	77,200[c]	>4,000	N/A	2.25
External Components		LC, electrodes Antenna Capacitor	LC, electrodes Antenna Off-chip ICs for powering and communication	LC, electrodes Antenna	L, electrodes Antenna	None
AFE	Input Ref. Noise [μV]	5.2	5.4	1	1.3	2.5
	NEF	1.8	N/A	4.5	4.8	4.0
ADC	Type	SAR	SAR	SAR	VCO	SAR
	Resolution [bits]	10	12	12	15	10
Stimulation	Max. Output Current [μA]	30	No	No	No	145
Wireless Powering	Frequency [MHz]	13.56	0.266	13.56	300	190
	Antenna	Off-chip	Off-chip	Off-chip	Off-chip	On-chip
Communication	Forward	OOK 401-406 MHz	Zigbee N/A	No	No	ASK 190 MHz
	Backward	OOK 401-406 MHz	IR-UWB 7.3-8.5 GHz	FSK 402-405 MHz	LSK 300 MHz	LSK 190 MHz

[a]8 recording channels and 2 stimulation channels. [b]Only for the data acquisition unit. [c]Only for the communication unit.

the miniaturized and enclosed ENIAC system permits no access to a distal ground electrode. As illustrated in Fig. 12(b), the ENIAC stimulator operates in two phases. During the first phase, constant complementary currents are provided through the differential capacitive electrodes. The ramping voltage adiabatic power rails V_{DD_STM} and V_{SS_STM} providing the complementary currents are generated directly from the LC tank utilizing a foldable stack of rectifiers. During the second phase energy is replenished by returning the charge stored on the electrode capacitors to the system V_{DD} and V_{SS} for reuse by other ENIAC modules. For triphasic rather than biphasic stimulation, as shown, the two phases are repeated but now with opposite polarity. This is accomplished by swapping the electrode connections through the switch matrix prior to executing the same two-phase sequence. Finally, the electrodes are shorted to even out any residual charge on the electrode capacitors.

Fig. 13 shows measured voltage and current waveform for the triphasic stimulation with a platinum model electrode, consistent with the model in Fig. 12(b), and showing 145 μA of current delivered per electrode channel. This is four times larger than other integrated ECoG systems even though no external components are used and system volume is substantially smaller (Table 2).

VI. CONCLUDING REMARKS

In this work, we highlighted the importance of high density electrocorticography for brain activity mapping, brain–computer interfaces, and treatments for neurological disorders. We reviewed the critical design challenges on fully implantable ECoG interface systems in their major aspects including electrode interface, recording and stimulation circuitry, wireless power and data communications. In addition, we surveyed state-of-the-art systems at the forefront of clinical and research applications and noted the rapid evolution of the technology in the past few years. Finally, we make the case for a new type of device that promises to expand the applications of implantable brain monitoring: modular μECoG. We demonstrate a new approach to miniaturization of modular μECoG with our fully integrated encapsulated neural interfacing acquisition chip (ENIAC). This system on a chip is capable of recording, stimulation, wireless power conditioning and bidirectional communication without the need for any external components. Its major specifications, performances, and functionalities are summarized in comparison with other state-of-the-art ECoG interface systems in Table 2. Having a fully integrated neural interface system, including electrodes and antenna is a new milestone for miniaturization that sets the stage for exciting clinical and research developments. ■

Acknowledgment

The authors would like to thank V. Gilja, S. Dayeh, E. Halgren, B. McNaughton, and J. Viventi for critical input and stimulating discussions on clinical and fundamental neuroscience applications of high-density ECoG neural interfaces.

REFERENCES

[1] The White House, "The BRAIN Initiative." [Online]. Available: https://www.whitehouse.gov/BRAIN

[2] The National Institute of Health, "BRAIN Working Group Report: BRAIN 2025—A Scientific Vision." [Online]. Available: http://braininitiative.nih.gov/2025/BRAIN2025.pdf

[3] P. L. Nunez, "Electric and magnetic fields produced by the brain," in *Brain-Computer Interfaces: Principles and Practice*, J. Wolpaw and E. W. Wolpaw, Eds. Oxford, U.K.: Oxford Univ. Press, 2012, pp. 171–212.

[4] R. B. Reilly, "Neurology: Central nervous system," in *The Physiological Measurement Handbook*, J. G. Webster, Ed. Boca Raton, FL, USA: CRC Press, 2014, pp. 171–212.

[5] M. Fukushima, Z. C. Chao, and N. Fujii, "Studying brain functions with mesoscopic measurements: Advances in electrocorticography for non-human primates," *Curr. Opinion Neurobiol.*, vol. 32, pp. 124–131, 2015.

[6] M. Hirata *et al.*, "A fully-implantable wireless system for human brain-machine interfaces using brain surface electrodes: W-HERBS," *IEICE Trans. Commun.*, vol. E94b, no. 9, pp. 2448–2453, 2011.

[7] H. Lee, R. V. Bellamkonda, W. Sun, and M. E. Levenston, "Biomechanical analysis of silicon microelectrode-induced strain in the brain," *J. Neural Eng.*, vol. 2, no. 4, p. 81, 2005.

[8] G. C. McConnell *et al.*, "Implanted neural electrodes cause chronic, local inflammation that is correlated with local neurodegeneration," *J. Neural Eng.*, vol. 6, no. 5, 2009, Art. no. 056003.

[9] L. Karumbaiah *et al.*, "Relationship between intracortical electrode design and chronic recording function," *Biomaterials*, vol. 34, no. 33, pp. 8061–8074, 2013.

[10] V. S. Polikov, P. A. Tresco, and W. M. Reichert, "Response of brain tissue to chronically implanted neural electrodes," *J. Neurosci. Methods*, vol. 148, no. 1, pp. 1–18, 2005.

[11] W. J. Freeman, L. J. Rogers, M. D. Holmes, and D. L. Silbergeld, "Spatial spectral analysis of human electrocorticograms including the alpha and gamma bands," *J. Neurosci. Methods*, vol. 95, no. 2, pp. 111–121, 2000.

[12] E. C. Leuthardt, Z. Freudenberg, D. Bundy, and J. Roland, "Microscale recording from human motor cortex: Implications for minimally invasive electrocorticographic brain-computer interfaces," *Neurosurgical Focus*, vol. 27, no. 1, p. E10, 2009.

[13] M. W. Slutzky *et al.*, "Optimal spacing of surface electrode arrays for brain-machine interface applications," *J. Neural Eng.*, vol. 7, no. 2, 2010, Art. no. 026004.

[14] R. J. Staba, C. L. Wilson, A. Bragin, I. Fried, and J. Engel, "Quantitative analysis of high-frequency oscillations (80–500 Hz) recorded in human epileptic hippocampus and entorhinal cortex," *J. Neurophysiol.*, vol. 88, no. 4, pp. 1743–1752, 2002.

[15] W. J. Freeman, M. D. Holmes, B. C. Burke, and S. Vanhatalo, "Spatial spectra of scalp EEG and EMG from awake humans," *Clin. Neurophysiol.*, vol. 114, no. 6, pp. 1053–1068, 2003.

[16] T. Ball, M. Kern, I. Mutschler, A. Aertsen, and A. Schulze-Bonhage, "Signal quality of simultaneously recorded invasive and non-invasive EEG," *NeuroImage*, vol. 46, no. 3, pp. 708–716, 2009.

[17] H. Berger, "Electroencephalogram in humans," *Archiv Fur Psychiatrie Und Nervenkrankheiten*, vol. 87, pp. 527–570, 1929.

[18] P. L. Nunez and R. Srinivasan, "Fallacies in EEG," in *Electric Fields of the Brain: The Neurophysics of EEG*, 2nd ed. New York, NY, USA: Oxford Univ. Press, 2006, ch. 2, pp. 56–98.

[19] P. L. Nunez and R. Srinivasan, "Electric fields and currents in biological tissue," in *Electric Fields of the Brain: The Neurophysics of EEG*, 2nd ed. New York, NY, USA: Oxford Univ. Press, 2006, ch. 4, pp. 147–202.

[20] E. C. Leuthardt, G. Schalk, J. R. Wolpaw, J. G. Ojemann, and D. W. Moran, "A brain-computer interface using electrocorticographic signals in humans," *J. Neural Eng.*, vol. 1, no. 2, p. 63, 2004.

[21] S. Kellis, B. Greger, S. Hanrahan, P. House, and R. Brown, "Platinum microwire for subdural electrocorticography over human neocortex: Millimeter-scale spatiotemporal dynamics," in *Proc. Annu. Int. Conf. IEEE Eng. Med. Biol. Soc.*, 2011, pp. 4761–4765.

[22] S. Kellis *et al.*, "Decoding hand trajectories from micro-electrocorticography in human patients," in *Proc. Annu. Int. Conf. IEEE Eng. Med. Biol. Soc.*, 2012, pp. 4091–4094.

[23] S. Morris *et al.*, "Patient-specific cortical electrodes for Sulcal and Gyral implantation," *IEEE Trans. Biomed. Eng.*, vol. 62, no. 4, pp. 1034–1041, 2015.

[24] B. Rubehn, C. Bosman, R. Oostenveld, P. Fries, and T. Stieglitz, "A MEMS-based flexible multichannel ECoG-electrode array," *J. Neural Eng.*, vol. 6, no. 3, 2009, Art. no. 036003.

[25] E. Tolstosheeva *et al.*, "A multi-channel, flex-rigid ECoG microelectrode array for visual cortical interfacing," *Sensors*, vol. 15, no. 1, pp. 832–854, 2015.

[26] F. Kohler, M. Schuettler, and T. Stieglitz, "Parylene-coated metal tracks for neural electrode arrays—Fabrication approaches and improvements utilizing different laser systems," in *Proc. Annu. Int. Conf. IEEE Eng. Med. Biol. Soc.*, 2012, pp. 5130–5133.

[27] T. J. Richner *et al.*, "Optogenetic micro-electrocorticography for modulating and localizing cerebral cortex activity," *J. Neural Eng.*, vol. 11, no. 1, 2014, Art. no. 016010.

[28] E. Castagnola *et al.*, "PEDOT-CNT-coated low-impedance, ultra-flexible, and brain-conformable micro-ECoG arrays," *IEEE Trans. Neural Syst. Rehabil. Eng.*, vol. 23, no. 3, pp. 342–350, 2015.

[29] D. H. Kim *et al.*, "Dissolvable films of silk fibroin for ultrathin conformal bio-integrated electronics," *Nature Mater.*, vol. 9, no. 6, pp. 511–517, 2010.

[30] J. Viventi *et al.*, "Flexible, foldable, actively multiplexed, high-density electrode array for mapping brain activity *in vivo*," *Nature Neurosci.*, vol. 14, no. 12, pp. 1599–U138, 2011.

[31] K. Y. Kwon, B. Sirowatka, A. Weber, and W. Li, "Opto-ECoG array: A hybrid neural interface with transparent ECoG electrode array and integrated LEDs for optogenetics," *IEEE Trans. Biomed. Circuits Syst.*, vol. 7, no. 5, pp. 593–600, 2013.

[32] S. Ha *et al.*, "Integrated circuits and electrode interfaces for noninvasive physiological monitoring," *IEEE Trans. Biomed. Eng.*, vol. 61, no. 5, pp. 1522–1537, 2014.

[33] R. Grech *et al.*, "Review on solving the inverse problem in EEG source analysis," *J. Neuroeng. Rehabil.*, vol. 5, 2008, doi: 10.1186/1743-0003-5-25.

[34] Y.-C. Chen *et al.*, "An active, flexible carbon nanotube microelectrode array for recording electrocorticograms," *J. Neural Eng.*, vol. 8, no. 3, 2011, Art. no. 034001.

[35] A. A. Schendel, K. W. Eliceiri, and J. C. Williams, "Advanced materials for neural surface electrodes," *Curr. Opinion Solid State Mater. Sci.*, vol. 18, no. 6, pp. 301–307, 2014.

[36] D. Khodagholy *et al.*, "In vivo recordings of brain activity using organic transistors," *Nature Commun.*, vol. 4, p. 1575, 2013.

[37] R. R. Harrison, "The design of integrated circuits to observe brain activity," *Proc. IEEE*, vol. 96, no. 7, pp. 1203–1216, 2008.

[38] X. Tong and M. Ghovanloo, "Multichannel wireless neural recording AFE architectures analysis, modeling, and tradeoffs," *IEEE Design Test*, vol. 33, no. 4, pp. 24–36, 2016.

[39] M. S. J. Steyaert, W. M. C. Sansen, and Z. Y. Chang, "A micropower low-noise monolithic instrumentation amplifier for medical purposes," *IEEE J. Solid-State Circuits*, vol. 22, no. 6, pp. 1163–1168, 1987.

[40] R. R. Harrison and C. Charles, "A low-power low-noise CMOS amplifier for neural recording applications," *IEEE J. Solid-State Circuits*, vol. 38, no. 6, pp. 958–965, 2003.

[41] T. Denison *et al.*, "A 2 μW 100 nV/rtHz chopper-stabilized instrumentation amplifier for chronic measurement of neural field potentials," *IEEE J. Solid-State Circuits*, vol. 42, no. 12, pp. 2934–2945, 2007.

[42] R. F. Yazicioglu, P. Merken, R. Puers, and C. Van Hoof, "A 60 μW 60 nV/rtHz readout front-end for portable biopotential acquisition systems," *IEEE J. Solid-State Circuits*, vol. 42, no. 5, pp. 1100–1110, 2007.

[43] R. F. Yazicioglu, P. Merken, R. Puers, and C. van Hoof, "A 200 μW eight-channel EEG acquisition ASIC for ambulatory EEG systems," *IEEE J.*

Solid-State Circuits, vol. 43, no. 12, pp. 3025–3038, 2008.

[44] M. Mollazadeh, K. Murari, G. Cauwenberghs, and N. Thakor, "Micropower CMOS integrated low-noise amplification, filtering, and digitization of multimodal neuropotentials," *IEEE Trans. Biomed. Circuits Syst.*, vol. 3, no. 1, pp. 1–10, 2009.

[45] R. Wu, K. A. A. Makinwa, and J. H. Huijsing, "A chopper current-feedback instrumentation amplifier with a 1 mHz $1/f$ noise corner and an ac-coupled ripple reduction loop," *IEEE J. Solid-State Circuits*, vol. 44, no. 12, pp. 3232–3243, 2009.

[46] X. Zou, X. Xu, L. Yao, and Y. Lian, "A 1-V 450-nW fully integrated programmable biomedical sensor interface chip," *IEEE J. Solid-State Circuits*, vol. 44, no. 4, pp. 1067–1077, 2009.

[47] N. Verma *et al.*, "A micro-power EEG acquisition SoC with integrated feature extraction processor for a chronic seizure detection system," *IEEE J. Solid-State Circuits*, vol. 45, no. 4, pp. 804–816, 2010.

[48] J. Xu *et al.*, "A 160 μW 8-channel active electrode system for EEG monitoring," *IEEE Trans. Biomed. Circuits Syst.*, vol. 5, no. 6, pp. 555–567, 2011.

[49] Q. W. Fan, F. Sebastiano, J. H. Huijsing, and K. A. A. Makinwa, "A 1.8 μW 60 nV/rtHz capacitively-coupled chopper instrumentation amplifier in 65 nm CMOS for wireless sensor nodes," *IEEE J. Solid-State Circuits*, vol. 46, no. 7, pp. 1534–1543, 2011.

[50] F. Zhang, J. Holleman, and B. P. Otis, "Design of ultra-low power biopotential amplifiers for biosignal acquisition applications," *IEEE Trans. Biomed. Circuits Syst.*, vol. 6, no. 4, pp. 344–355, 2012.

[51] Y. Tseng, Y. C. Ho, S. T. Kao, and C. C. Su, "A 0.09 μW low power front-end biopotential amplifier for biosignal recording," *IEEE Trans. Biomed. Circuits Syst.*, vol. 6, no. 5, pp. 508–516, 2012.

[52] J. Yoo *et al.*, "An 8-channel scalable EEG acquisition SoC with patient-specific seizure classification and recording processor," *IEEE J. Solid-State Circuits*, vol. 48, no. 1, pp. 214–228, 2013.

[53] B. Johnson and A. Molnar, "An orthogonal current-reuse amplifier for multi-channel sensing," *IEEE J. Solid-State Circuits*, vol. 48, no. 6, pp. 1487–1496, 2013.

[54] D. Han, Y. Zheng, R. Rajkumar, G. S. Dawe, and M. Je, "A 0.45 V 100-channel neural-recording IC with sub-μW/channel consumption in 0.18 μm CMOS," *IEEE Trans. Biomed. Circuits Syst.*, vol. 7, no. 6, pp. 735–746, 2013.

[55] Y. Chen *et al.*, "A digitally assisted, signal folding neural recording amplifier," *IEEE Trans. Biomed. Circuits Syst.*, vol. 8, no. 4, pp. 528–542, 2014.

[56] T.-Y. Wang, M.-R. Lai, C. M. Twigg, and S.-Y. Peng, "A fully reconfigurable low-noise biopotential sensing amplifier with 1.96 noise efficiency factor," *IEEE Trans. Biomed. Circuits Syst.*, vol. 8, no. 3, pp. 411–422, 2014.

[57] P. Harpe, G. Hao, R. van Dommele, E. Cantatore, and A. van Roermund, "21.2 A 3 nW signal-acquisition IC integrating an amplifier with 2.1 NEF and a 1.5 fJ/conv-step ADC," in *IEEE Int. Solid-State Circuits Conf. Dig. Tech. Papers*, 2015, pp. 1–3.

[58] S. Song *et al.*, "A low-voltage chopper-stabilized amplifier for fetal ECG monitoring with a 1.41 power efficiency factor," *IEEE Trans. Biomed. Circuits Syst.*, vol. 9, no. 2, pp. 237–247, 2015.

[59] T. Yang and J. Holleman, "An ultralow-power low-noise CMOS biopotential amplifier for neural recording," *IEEE Trans. Circuits Syst. II, Exp. Briefs*, vol. 62, no. 10, pp. 927–931, 2015.

[60] R. Sarpeshkar, *Ultra Low Power Bioelectronics: Fundamentals, Biomedical Applications, and Bio-Inspired Systems*. Cambridge, U.K.: Cambridge Univ. Press, 2010.

[61] S. Ha, C. Kim, Y. M. Chi, and G. Cauwenberghs, "Low-Power Integrated Circuit Design for Wearable Biopotential Sensing," in *Wearable Sensors*, E. Sazonov and M. R. Neuman, Eds. Oxford, U.K.: Academic, 2014, pp. 323–352.

[62] C. C. Enz and G. C. Temes, "Circuit techniques for reducing the effects of op-amp imperfections: Autozeroing, correlated double sampling, and chopper stabilization," *Proc. IEEE*, vol. 84, no. 11, pp. 1584–1614, 1996.

[63] C. Menolfi and Q. T. Huang, "A low-noise CMOS instrumentation amplifier for thermoelectric infrared detectors," *IEEE J. Solid-State Circuits*, vol. 32, no. 7, pp. 968–976, 1997.

[64] W. Smith, B. Mogen, E. Fetz, and B. Otis, "A spectrum-equalizing analog front end for low-power electrocorticography recording," in *Proc. IEEE Eur. Solid State Circuits Conf.*, 2014, pp. 107–110.

[65] S.-Y. Park, J. Cho, K. Na, and E. Yoon, "Toward 1024-channel parallel neural recording: Modular $\Delta - \Delta\Sigma$ AFE architecture with 4.84 fj/c-s $\cdot$ mm^2 energy-area product," in *Proc. Symp. VLSI Circuits Dig. Tech. Papers*, 2015, pp. C112–C113.

[66] R. Muller *et al.*, "A minimally invasive 64-channel wireless μECoG implant," *IEEE J. Solid-State Circuits*, vol. 50, no. 1, pp. 344–359, 2015.

[67] R. R. Harrison *et al.*, "A low-power integrated circuit for a wireless 100-electrode neural recording system," *IEEE J. Solid-State Circuits*, vol. 42, no. 1, pp. 123–133, 2007.

[68] J. N. Y. Aziz *et al.*, "256-channel neural recording and delta compression microsystem with 3D electrodes," *IEEE J. Solid-State Circuits*, vol. 44, no. 3, pp. 995–1005, 2009.

[69] H. Gao *et al.*, "HermesE: A 96-channel full data rate direct neural interface in 0.13 μm CMOS," *IEEE J. Solid-State Circuits*, vol. 47, no. 4, pp. 1043–1055, 2012.

[70] R. Shulyzki *et al.*, "320-channel active probe for high-resolution neuromonitoring and responsive neurostimulation," *IEEE Trans. Biomed. Circuits Syst.*, vol. 9, no. 1, pp. 34–49, 2015.

[71] L. Yan *et al.*, "A 680 nA ECG acquisition IC for leadless pacemaker applications," *IEEE Trans. Biomed. Circuits Syst.*, vol. 8, no. 6, pp. 779–786, 2014.

[72] W. Penfield and E. Boldrey, "Somatic motor and sensory representation in the cerebral cortex of man as studied by electrical stimulation," *Brain*, vol. 60, no. 4, pp. 389–443, 1937.

[73] L. Mazzola, J. Isnard, R. Peyron, and F. Mauguière, "Stimulation of the human cortex and the experience of pain: Wilder Penfield's observations revisited," *Brain*, vol. 135, no. 2, pp. 631–640, 2012.

[74] A. Berényi, M. Belluscio, D. Mao, and G. Buzsáki, "Closed-loop control of epilepsy by transcranial electrical stimulation," *Science*, vol. 337, no. 6095, pp. 735–737, 2012.

[75] D. J. Mogul and W. van Drongelen, "Electrical control of epilepsy," *Annu. Rev. Biomed. Eng.*, vol. 16, pp. 483–504, 2014.

[76] L. A. Johnson *et al.*, "Direct electrical stimulation of the somatosensory cortex in humans using electrocorticography electrodes: A qualitative and quantitative report," *J. Neural Eng.*, vol. 10, no. 3, 2013, Art. no. 036021.

[77] W.-M. Chen *et al.*, "A fully integrated 8-channel closed-loop neural-prosthetic CMOS SOC for real-time epileptic seizure control," *IEEE J. Solid-State Circuits*, vol. 49, no. 1, pp. 232–247, 2014.

[78] S. Borchers, M. Himmelbach, N. Logothetis, and H. O. Karnath, "Direct electrical stimulation of human cortex—The gold standard for mapping brain functions?" *Nature Rev. Neurosci.*, vol. 13, no. 1, pp. 63–70, 2012.

[79] B. Jarosiewicz *et al.*, "Advantages of closed-loop calibration in intracortical brain-computer interfaces for people with tetraplegia," *J. Neural Eng.*, vol. 10, no. 4, 2013, Art. no. 046012.

[80] R. Levy *et al.*, "Cortical stimulation for the rehabilitation of patients with hemiparetic stroke: A multicenter feasibility study of safety and efficacy," *J. Neurosurgery*, vol. 108, no. 4, pp. 707–714, 2008.

[81] M. A. Edwardson, T. H. Lucas, J. R. Carey, and E. E. Fetz, "New modalities of brain stimulation for stroke rehabilitation," *Exp. Brain Res.*, vol. 224, no. 3, pp. 335–358, 2013.

[82] P. M. Lewis, H. M. Ackland, A. J. Lowery, and J. V. Rosenfeld, "Restoration of vision in blind individuals using bionic devices: A review with a focus on cortical visual prostheses," *Brain Res.*, vol. 1595, pp. 51–73, 2015.

[83] F. Caruana *et al.*, "Mirth and laughter elicited by electrical stimulation of the human anterior cingulate cortex," *Cortex*, vol. 71, pp. 323–331, 2015.

[84] M. Ortmanns, A. Rocke, M. Gehrke, and H. J. Tiedtke, "A 232-channel epiretinal stimulator ASIC," *IEEE J. Solid-State Circuits*, vol. 42, no. 12, pp. 2946–2959, 2007.

[85] C. Kuanfu *et al.*, "An integrated 256-channel epiretinal prosthesis," *IEEE J. Solid-State Circuits*, vol. 45, no. 9, pp. 1946–1956, 2010.

[86] Y.-K. Lo, K. Chen, P. Gad, and W. Liu, "A fully-integrated high-compliance voltage SoC for epi-retinal and neural prostheses," *IEEE Trans. Biomed. Circuits Syst.*, vol. 7, no. 6, pp. 761–772, 2013.

[87] W. Biederman *et al.*, "A 4.78 mm^2 fully-integrated neuromodulation SoC combining 64 acquisition channels with digital compression and simultaneous dual stimulation," *IEEE J. Solid-State Circuits*, vol. 50, no. 4, pp. 1038–1047, 2015.

[88] S. Ha *et al.*, "A 16-channel wireless neural interfacing SoC with RF-powered energy-replenishing adiabatic stimulation," in *Proc. Symp. VLSI Circuits Dig. Tech. Papers*, 2015, pp. C106–C107.

[89] S. K. Kelly and J. L. Wyatt, "A power-efficient neural tissue stimulator with energy recovery," *IEEE Trans. Biomed. Circuits Syst.*, vol. 5, no. 1, pp. 20–29, 2011.

[90] S. K. Arfin and R. Sarpeshkar, "An energy-efficient, adiabatic electrode stimulator with inductive energy recycling and feedback current regulation," *IEEE Trans. Biomed. Circuits Syst.*, vol. 6, no. 1, pp. 1–14, 2012.

[91] A. Rothermel *et al.*, "A 1600-pixel subretinal chip with dc-free terminals and ± 2 V supply optimized for long lifetime and high stimulation efficiency," in *Proc. IEEE Int. Solid-State Circuits Conf. Dig. Tech. Papers*, 2008, pp. 144–145.

[92] B. K. Thurgood, D. J. Warren, N. M. Ledbetter, G. A. Clark, and R. R. Harrison, "A wireless integrated circuit for 100-channel charge-balanced neural stimulation," *IEEE Trans. Biomed. Circuits Syst.*, vol. 3, no. 6, pp. 405–414, 2009.

[93] M. Monge *et al.*, "A fully intraocular high-density self-calibrating epiretinal prosthesis," *IEEE Trans. Biomed. Circuits Syst.*, vol. 7, no. 6, pp. 747–760, 2013.

[94] M. Sivaprakasam, L. Wentai, M. S. Humayun, and J. D. Weiland, "A variable range bi-phasic current stimulus driver circuitry for an implantable retinal prosthetic device," *IEEE J. Solid-State Circuits*, vol. 40, no. 3, pp. 763–771, 2005.

[95] M. Yip, J. Rui, H. H. Nakajima, K. M. Stankovic, and A. P. Chandrakasan, "A fully-implantable cochlear implant SoC with piezoelectric middle-ear sensor and arbitrary waveform neural stimulation," *IEEE J. Solid-State Circuits*, vol. 50, no. 1, pp. 214–229, 2015.

[96] D. R. Merrill, M. Bikson, and J. G. R. Jefferys, "Electrical stimulation of excitable tissue: Design of efficacious and safe protocols," *J. Neurosci. Methods*, vol. 141, no. 2, pp. 171–198, 2005.

[97] C. Q. Huang, R. K. Shepherd, P. M. Carter, P. M. Seligman, and B. Tabor, "Electrical stimulation of the auditory nerve: Direct current measurement in vivo," *IEEE Trans. Biomed. Eng.*, vol. 46, no. 4, pp. 461–470, 1999.

[98] G. J. Suaning and N. H. Lovell, "CMOS neurostimulation ASIC with 100 channels, scaleable output, and bidirectional radio-frequency telemetry," *IEEE Trans. Biomed. Eng.*, vol. 48, no. 2, pp. 248–260, 2001.

[99] S. K. Arfin, M. A. Long, M. S. Fee, and R. Sarpeshkar, "Wireless neural stimulation in freely behaving small animals," *J. Neurophysiol.*, vol. 102, no. 1, pp. 598–605, 2009.

[100] I. Schoen and P. Fromherz, "Extracellular stimulation of mammalian neurons through repetitive activation of Na^+ channels by weak capacitive currents on a silicon chip," *J. Neurophysiol.*, vol. 100, no. 1, pp. 346–357, 2008.

[101] A. Lambacher *et al.*, "Identifying firing mammalian neurons in networks with high-resolution multi-transistor array (MTA)," *Appl. Phys. A, Mater. Sci. Process.*, vol. 102, no. 1, pp. 1–11, 2011.

[102] W. Liu *et al.*, "A neuro-stimulus chip with telemetry unit for retinal prosthetic device," *IEEE J. Solid-State Circuits*, vol. 35, no. 10, pp. 1487–1497, 2000.

[103] J.-J. Sit and R. Sarpeshkar, "A low-power blocking-capacitor-free charge-balanced electrode-stimulator chip with less than 6 nA dc error for 1-mA full-scale stimulation," *IEEE Trans. Biomed. Circuits Syst.*, vol. 1, no. 3, pp. 172–183, 2007.

[104] E. Noorsal *et al.*, "A neural stimulator frontend with high-voltage compliance and programmable pulse shape for epiretinal implants," *IEEE J. Solid-State Circuits*, vol. 47, no. 1, pp. 244–256, 2012.

[105] K. Sooksood, T. Stieglitz, and M. Ortmanns, "An active approach for charge balancing in functional electrical stimulation," *IEEE Trans. Biomed. Circuits Syst.*, vol. 4, no. 3, pp. 162–170, 2010.

[106] E. Greenwald, C. Cheng, N. Thakor, C. Maier, and G. Cauwenberghs, "A CMOS neurostimulator with on-chip DAC calibration and charge balancing," in *Proc. IEEE Biomed. Circuits Syst. Conf.*, 2013, pp. 89–92.

[107] F. D. Broccard *et al.*, "Closed-loop brain-machine-body interfaces for noninvasive rehabilitation of movement disorders," *Ann. Biomed. Eng.*, vol. 42, no. 8, pp. 1573–1593, 2014.

[108] T. Denison, M. Morris, and F. Sun, "Building a bionic nervous system," *IEEE Spectrum*, vol. 52, no. 2, pp. 32–39, 2015.

[109] P. R. Gigante and R. R. Goodman, "Responsive neurostimulation for the treatment of epilepsy," *Neurosurgery Clin. North Amer.*, vol. 22, no. 4, pp. 477–80, vi, 2011.

[110] C. N. Heck *et al.*, "Two-year seizure reduction in adults with medically intractable partial onset epilepsy treated with responsive neurostimulation: Final results of the RNS System Pivotal trial," *Epilepsia*, vol. 55, no. 3, pp. 432–441, 2014.

[111] M. J. Cook *et al.*, "Prediction of seizure likelihood with a long-term, implanted seizure advisory system in patients with drug-resistant epilepsy: A first-in-man study," *Lancet Neurol.*, vol. 12, no. 6, pp. 563–571, 2013.

[112] M. Bandarabadi and A. Dourado, "A robust low complexity algorithm for real-time epileptic seizure detection," *Epilepsia*, vol. 55, pp. 137–137, 2014.

[113] S. Ramgopal *et al.*, "Seizure detection, seizure prediction, and closed-loop warning systems in epilepsy," *Epilepsy Behav.*, vol. 37, pp. 291–307, 2014.

[114] Z. Zhang and K. K. Parhi, "Low-complexity seizure prediction from iEEG/sEEG using spectral power and ratios of spectral power," *IEEE Trans. Biomed. Circuits Syst.*, vol. 10, no. 3, pp. 693–706, 2016.

[115] K. Abdelhalim, H. M. Jafari, L. Kokarovtseva, J. L. Perez Velazquez, and R. Genov, "4-channel uwb wireless neural vector analyzer soc with a closed-loop phase synchrony-triggered neurostimulator," *IEEE J. Solid-State Circuits*, vol. 48, no. 10, pp. 2494–2510, 2013.

[116] J. Yoo *et al.*, "An 8-channel scalable EEG acquisition SoC with patient-specific seizure classification and recording processor," *IEEE J. Solid-State Circuits*, vol. 48, no. 1, pp. 214–228, 2013.

[117] A. Page *et al.*, "A flexible multichannel EEG feature extractor and classifier for seizure detection," *IEEE Trans. Circuits Syst. II, Exp. Briefs*, vol. 62, no. 2, pp. 109–113, 2015.

[118] A. M. Bin Altaf, Z. Chen, and J. Yoo, "A 16-channel patient-specific seizure onset and termination detection soc with impedance-adaptive transcranial electrical stimulator," *IEEE J. Solid-State Circuits*, vol. 50, no. 11, pp. 2728–2740, 2015.

[119] G. Schalk and E. C. Leuthardt, "Brain-computer interfaces using electrocorticographic signals," *IEEE Rev. Biomed. Eng.*, vol. 4, pp. 140–154, 2011.

[120] A. T. Avestruz *et al.*, "A 5 μW/channel spectral analysis IC for chronic bidirectional brain-machine interfaces," *IEEE J. Solid-State Circuits*, vol. 43, no. 12, pp. 3006–3024, 2008.

[121] F. Zhang, A. Mishra, A. G. Richardson, and B. Otis, "A low-power ECoG/EEG processing IC with integrated multiband energy extractor," *IEEE Trans. Circuits Syst. I, Reg. Papers*, vol. 58, no. 9, pp. 2069–2082, 2011.

[122] C. S. Mestais *et al.*, "WIMAGINE: Wireless 64-channel ECoG recording implant for long term clinical applications," *IEEE Trans. Neural Syst. Rehabil. Eng.*, vol. 23, no. 1, pp. 10–21, 2015.

[123] A. M. Sodagar, G. E. Perlin, Y. Ying, K. Najafi, and K. D. Wise, "An implantable 64-channel wireless microsystem for single-unit neural recording," *IEEE J. Solid-State Circuits*, vol. 44, no. 9, pp. 2591–2604, 2009.

[124] A. M. Sodagar, K. D. Wise, and K. Najafi, "A wireless implantable microsystem for multichannel neural recording," *IEEE Trans. Microw. Theory Tech.*, vol. 57, no. 10, pp. 2565–2573, 2009.

[125] F. Goodarzy, E. Skafidas, and S. Gambini, "Feasibility of energy-autonomous wireless micro-sensors for biomedical applications: Powering and communication," *IEEE Rev. Biomed. Eng.*, vol. 8, pp. 17–29, 2015.

[126] A. Kim, M. Ochoa, R. Rahimi, and B. Ziaie, "New and emerging energy sources for implantable wireless microdevices," *IEEE Access*, vol. 3, pp. 89–98, 2015.

[127] J. P. Reilly, *Applied Bioelectricity, From Electrical Stimulation to Electropathology*. New York, NY, USA: Springer-Verlag, 1998.

[128] D. Miklavčič, N. Pavšelj, and F. X. Hart, "Electric properties of tissues," in *Wiley Encyclopedia of Biomedical Engineering*. New York, NY, USA: Wiley, 2006.

[129] C. Gabriel and S. Gabriel, "Compilation of the dielectric properties of body tissues at RF and microwave frequencies." [Online]. Available: http://niremf.ifac.cnr.it/docs/DIELECTRIC/home.html

[130] K. Murakawa, M. Kobayashi, O. Nakamura, and S. Kawata, "A wireless near-infrared energy system for medical implants," *IEEE Eng. Med. Biol. Mag.*, vol. 18, no. 6, pp. 70–72, 1999.

[131] K. Goto, T. Nakagawa, O. Nakamura, and S. Kawata, "An implantable power supply with an optically rechargeable lithium battery," *IEEE Trans. Biomed. Eng.*, vol. 48, no. 7, pp. 830–833, 2001.

[132] C. Algora and R. Pěna, "Recharging the battery of implantable biomedical devices by light," *Artif. Organs*, vol. 33, no. 10, pp. 855–860, 2009.

[133] T.-C. Chou, R. Subramanian, J. Park, and P. P. Mercier, "A miniaturized ultrasonic power delivery system," in *Proc. IEEE Biomed. Circuits Syst. Conf.*, 2014, pp. 440–443.

[134] D. Seo *et al.*, "Ultrasonic beamforming system for interrogating multiple implantable sensors," in *Proc. Annu. Int. Conf. IEEE Eng. Med. Biol. Soc.*, 2015, pp. 2673–2676.

[135] F.-G. Zeng, S. Rebscher, W. Harrison, X. Sun, and H. Feng, "Cochlear implants: System design, integration, and evaluation," *IEEE Rev. Biomed. Eng.*, vol. 1, pp. 115–142, 2008.

[136] H.-M. Lee, K. Y. Kwon, L. Wen, and M. Ghovanloo, "A power-efficient switched-capacitor stimulating system for electrical/optical deep brain stimulation," *IEEE J. Solid-State Circuits*, vol. 50, no. 1, pp. 360–374, 2015.

[137] B. M. Badr, R. Somogyi-Gsizmazia, K. R. Delaney, and N. Dechev, "Wireless power transfer for telemetric devices with variable orientation, for small rodent behavior monitoring," *IEEE Sensors J.*, vol. 15, no. 4, pp. 2144–2156, 2015.

[138] R. Jegadeesan, S. Nag, K. Agarwal, N. V. Thakor, and G. Yong-Xin, "Enabling wireless powering and telemetry for peripheral nerve implants," *IEEE J. Biomed. Health Inf.*, vol. 19, no. 3, pp. 958–970, 2015.

[139] O. Knecht, R. Bosshard, and J. W. Kolar, "High-efficiency transcutaneous energy transfer for implantable mechanical heart support systems," *IEEE Trans. Power Electron.*, vol. 30, no. 11, pp. 6221–6236, 2015.

[140] M. W. Baker and R. Sarpeshkar, "Feedback analysis and design of RF power links for low-power bionic systems," *IEEE Trans. Biomed. Circuits Syst.*, vol. 1, no. 1, pp. 28–38, 2007.

[141] U.-M. Jow and M. Ghovanloo, "Design and optimization of printed spiral coils for efficient transcutaneous inductive power transmission," *IEEE Trans. Biomed. Circuits Syst.*, vol. 1, no. 3, pp. 193–202, 2007.

[142] A. K. RamRakhyani, S. Mirabbasi, and C. Mu, "Design and optimization of resonance-based efficient wireless power delivery systems for biomedical implants," *IEEE Trans. Biomed. Circuits Syst.*, vol. 5, no. 1, pp. 48–63, 2011.

[143] R. F. Xue, K. W. Cheng, and M. Je, "High-efficiency wireless power transfer for biomedical implants by optimal resonant load transformation," *IEEE Trans. Circuits systems I. Reg. Papers*, vol. 60, no. 4, pp. 867–874, 2013.

[144] I. Mayordomo, T. Drager, P. Spies, J. Bernhard, and A. Pflaum, "An overview of technical challenges and advances of inductive wireless power transmission," *Proc. IEEE*, vol. 101, no. 6, pp. 1302–1311, 2013.

[145] H. Xu, J. Handwerker, and M. Ortmanns, "Telemetry for implantable medical devices: Part 2—Power telemetry," *IEEE Solid-State Circuits Mag.*, vol. 6, no. 3, pp. 60–63, 2014.

[146] D. Ahn and M. Ghovanloo, "Optimal design of wireless power transmission links for millimeter-sized biomedical implants," *IEEE Trans. Biomed. Circuits Syst.*, vol. 10, no. 1, pp. 125–137, 2016.

[147] M. Zargham and P. G. Gulak, "Fully integrated on-chip coil in 0.13 μm CMOS for wireless power transfer through biological media," *IEEE Trans. Biomed. Circuits Syst.*, vol. 9, no. 2, pp. 259–271, 2015.

[148] A. S. Y. Poon, S. O'Driscoll, and T. H. Meng, "Optimal frequency for wireless power transmission into dispersive tissue," *IEEE Trans. Antennas Propag.*, vol. 58, no. 5, pp. 1739–1750, 2010.

[149] M. Zargham and P. G. Gulak, "Maximum achievable efficiency in near-field coupled power-transfer systems," *IEEE Trans. Biomed. Circuits Syst.*, vol. 6, no. 3, pp. 228–245, 2012.

[150] F. T. Sun, M. J. Morrell, and R. E. Wharen, "Responsive cortical stimulation for the treatment of epilepsy," *Neurotherapeutics*, vol. 5, no. 1, pp. 68–74, 2008.

[151] "NeuroPace RNS System." [Online]. Available: http://www.neuropace.com/

[152] D. Prutchi, "Neurovista publishes study results for their implantable seizure-warning device." [Online]. Available: http://www.implantable-device.com

[153] K. A. Davis *et al.*, "A novel implanted device to wirelessly record and analyze continuous intracranial canine EEG," *Epilepsy Res.*, vol. 96, no. 1/2, pp. 116–122, 2011.

[154] A. G. Rouse *et al.*, "A chronic generalized bi-directional brain-machine interface," *J. Neural Eng.*, vol. 8, no. 3, 2011, Art. no. 036018.

[155] P. Afshar *et al.*, "A translational platform for prototyping closed-loop neuromodulation systems," *Front. Neural Circuits*, vol. 6, pp. 1–15, 2013, doi: 10.3389/fncir.2012.00117.

[156] M. Schuettler, F. Kohler, J. S. Ordonez, and T. Stieglitz, "Hermetic electronic packaging of an implantable brain-machine-interface with transcutaneous optical data communication," in *Proc. Annu. Int. Conf. IEEE Eng. Med. Biol. Soc.*, 2012, pp. 3886–3889.

[157] F. Kohler, M. A. Ulloa, J. S. Ordonez, T. Stieglitz, and M. Schuettler, "Reliability investigations and improvements of interconnection technologies for the wireless brain-machine interface —'BrainCon'," in *Proc. Int. IEEE/EMBS Conf. Neural Eng.*, 2013, pp. 1013–1016.

[158] J. D. Fischer, The braincon platform software? A closed-loop brain-computer interface software for research and medical applications, 2014.

[159] M. Hirata and T. Yoshimine, "Electrocorticographic brain-machine interfaces for motor and communication control," in *Clinical Systems Neuroscience*, K. Kansaku, L. G. Cohen, and N. Birbaumer, Eds. Japan: Springer-Verlag, 2015, ch. 5, pp. 83–100.

[160] "High-density microelectrocorticography array." [Online]. Available: http://corteraneuro.com/products/neuroscience

[161] R. Mohammadi *et al.*, "A compact ECoG system with bidirectional capacitive data telemetry," in *Proc. IEEE Biomed. Circuits Syst. Conf.*, 2014, pp. 600–603.

[162] G. A. DeMichele, S. F. Cogan, P. R. Troyk, H. Chen, and Z. Hu, "Multichannel wireless ECoG array ASIC devices," in *Proc. Annu. Int. Conf. IEEE Eng. Med. Biol. Soc.*, 2014, pp. 3969–3972.

[163] A. Ghomashchi *et al.*, "A low-cost, open-source, wireless electrophysiology system," in *Proc. Annu. Int. Conf. IEEE Eng. Med. Biol. Soc.*, 2014, pp. 3138–3141.

[164] P. P. Mercier and A. P. Chandrakasan, Eds., *Ultra-Low-Power Short-Range Radios*. New York, NY, USA: Springer-Verlag, 2015.

[165] A. P. Chandrakasan *et al.*, "Low-power impulse UWB architectures and circuits," *Proc. IEEE*, vol. 97, no. 2, pp. 332–352, 2009.

[166] P. P. Mercier, D. C. Daly, and A. P. Chandrakasan, "An energy-efficient all-digital UWB transmitter employing dual capacitively-coupled pulse-shaping drivers," *IEEE J. Solid-State Circuits*, vol. 44, no. 6, pp. 1679–1688, 2009.

[167] H. Ando *et al.*, "Wireless multichannel neural recording with a 128 Mbps UWB transmitter for implantable brain-machine interfaces," *IEEE Trans. Biomed. Circuits Syst.*, 2015, doi: 10.1109/TBCAS.2016.2514522.

[168] S. A. Mirbozorgi, H. Bahrami, M. Sawan, L. A. Rusch, and B. Gosselin, "A single-chip full-duplex high speed transceiver for multi-site stimulating and recording neural implants," *IEEE Trans. Biomed. Circuits Syst.*, vol. 10, no. 3, pp. 643–653, 2016.

[169] Z. Tang, B. Smith, J. H. Schild, and P. H. Peckham, "Data transmission from an implantable biotelemeter by load-shift keying using circuit configuration modulator," *IEEE Trans. Biomed. Eng.*, vol. 42, no. 5, pp. 524–528, 1995.

[170] C. Sauer, M. Stanacevic, G. Cauwenberghs, and N. Thakor, "Power harvesting and telemetry in CMOS for implanted devices," *IEEE Trans. Circuits Syst. I, Reg. Papers*, vol. 52, no. 12, pp. 2605–2613, 2005.

[171] S. Mandal and R. Sarpeshkar, "Power-efficient impedance-modulation wireless data links for biomedical implants," *IEEE Trans. Biomed. Circuits Syst.*, vol. 2, no. 4, pp. 301–315, 2008.

[172] H.-M. Lee and M. Ghovanloo, "An integrated power-efficient active rectifier with offset-controlled high speed comparators for inductively powered applications," *IEEE Trans. Circuits Syst. I, Reg. Papers*, vol. 58, no. 8, pp. 1749–1760, 2011.

[173] S. Ha, C. Kim, J. Park, S. Joshi, and G. Cauwenberghs, "Energy-recycling integrated 6.78-Mbps data 6.3-mW power telemetry over a single 13.56-MHz inductive link," in *IEEE Symp. VLSI Circuits Dig. Tech. Papers*, 2014, pp. 66–67.

[174] B. S. Wilson and M. F. Dorman, "Cochlear implants: A remarkable past and a brilliant future," *Hearing Res.*, vol. 242, no. 1/2, pp. 3–21, 2008.

[175] H. Bhamra *et al.*, "A 24 μW batteryless, crystal-free, multinode synchronized SoC "bionode" for wireless prosthesis control," *IEEE J. Solid-State Circuits*, vol. 50, no. 11, pp. 2714–2727, 2015.

[176] A. Yakovlev, J. H. Jang, and D. Pivonka, "An 11 μW sub-pJ/bit reconfigurable transceiver for mm-sized wireless implants," *IEEE Trans. Biomed. Circuits Syst.*, vol. 10, no. 1, pp. 175–185, 2016.

[177] Y. P. Lin *et al.*, "A battery-less, implantable neuro-electronic interface for studying the mechanisms of deep brain stimulation in rat models," *IEEE Trans. Biomed. Circuits Syst.*, vol. 10, no. 1, pp. 98–112, 2016.

[178] Z. Xiao *et al.*, "An implantable RFID sensor tag toward continuous glucose monitoring," *IEEE J. Biomed. Health Inf.*, vol. 19, no. 3, pp. 910–919, 2015.

[179] H. Yu and K. Najafi, "Low-power interface circuits for bio-implantable microsystems,"

in *Proc. IEEE Int. Solid-State Circuits Conf. Dig. Tech. Papers*, 2003, pp. 194–487.

[180] H.-M. Lee, H. Park, and M. Ghovanloo, "A power-efficient wireless system with adaptive supply control for deep brain stimulation," *IEEE J. Solid-State Circuits*, vol. 48, no. 9, pp. 2203–2216, 2013.

[181] G. Jiang and D. D. Zhou, "Technology advances and challenges in hermetic packaging for implantable medical devices," in *Implantable Neural Prostheses 2: Techniques and Engineering Approaches*, D. Zhou and E. Greenbaum, Eds. New York, NY: Springer-Verlag, 2010, pp. 27–61.

[182] A. Vanhoestenberghe and N. Donaldson, "Corrosion of silicon integrated circuits and lifetime predictions in implantable electronic devices," *J. Neural Eng.*, vol. 10, no. 3, 2013, Art. no. 031002.

[183] A. C. Ho *et al.*, "Long-term results from an epiretinal prosthesis to restore sight to the blind," *Ophthalmology*, vol. 122, no. 8, pp. 1547–1554, 2015.

[184] A. A. Weaver, K. L. Loftis, J. C. Tan, S. M. Duma, and J. D. Stitzel, "CT based three-dimensional measurement of orbit and eye anthropometry," *Investigative Ophthalmol. Visual Sci.*, vol. 51, no. 10, pp. 4892–4897, 2010.

[185] J. Jeong *et al.*, "A miniaturized, eye-conformable, and long-term reliable retinal prosthesis using monolithic fabrication of liquid crystal polymer (LCP)," *IEEE Trans. Biomed. Eng.*, vol. 62, no. 3, pp. 982–989, 2015.

[186] J. D. Weiland and M. S. Humayun, "Retinal prosthesis," *IEEE Trans. Biomed. Eng.*, vol. 61, no. 5, pp. 1412–1424, 2014.

[187] J. D. Weiland *et al.*, "Chip-scale packaging for bioelectronic implants," in *Proc. Int. IEEE/EMBS Conf. Neural Eng.*, 2013, pp. 931–936.

[188] S.-W. Hwang *et al.*, "A physically transient form of silicon electronics," *Science*, vol. 337, no. 6102, pp. 1640–1644, 2012.

[189] K. J. Yu *et al.*, "Bioresorbable silicon electronics for transient spatiotemporal mapping of electrical activity from the cerebral cortex," *Nature Mater.*, 2016, doi: 10.1038/nmat4624.

[190] C. Kim *et al.*, "A 144MHz integrated resonant regulating rectifier with hybrid pulse modulation," in *Proc. Symp. VLSI Circuits Dig. Tech. Papers*, 2015, pp. C284–C285.

[191] F. T. Sun and M. J. Morrell, "The RNS system: Responsive cortical stimulation for the treatment of refractory partial epilepsy," *Expert Rev. Med. Devices*, vol. 11, no. 6, pp. 563–572, 2014.

[192] C. N. Heck *et al.*, "Two-year seizure reduction in adults with medically intractable partial onset epilepsy treated with responsive neurostimulation: Final results of the RNS System Pivotal trial," *Epilepsia*, vol. 55, no. 3, pp. 432–441, 2014.

[193] S. Robinet *et al.*, "A low-power 0.7 μV_{rms} 32-channel mixed-signal circuit for ECoG recordings," *IEEE J. Emerging Sel. Top. Circuits Syst.*, vol. 1, no. 4, pp. 451–460, 2011.

[194] J. Jian and M. Stanaćević, "Optimal position of the transmitter coil for wireless power transfer to the implantable device," in *Proc. Annu. Int. Conf. IEEE Eng. Med. Biol. Soc.*, 2014, pp. 6549–6552.

[195] C. Kim *et al.*, "A fully integrated 144 MHz wireless-power-receiver-on-chip with an adaptive buck-boost regulating rectifier and low-loss h-tree signal distribution," in *Proc. Symp. VLSI Circuits Dig. Tech. Papers*, 2016, pp. C94–C95.

[196] T. Delbruck and C. A. Mead, "Adaptive photoreceptor with wide dynamic range," in *Proc. IEEE Int. Symp. Circuits Syst.*, vol. 4, 1994, pp. 339–342.

[197] H. Ando *et al.*, "Multichannel neural recording with a 128 Mbps UWB wireless transmitter for implantable brain-machine interfaces," in *Proc. Annu. Int. Conf. IEEE Eng. Med. Biol. Soc.*, 2015, pp. 4097–4100.

[198] T. Bjorninen *et al.*, "Design of wireless links to implanted brain-machine interface microelectronic systems," *IEEE Antennas Wireless Propag. Lett.*, vol. 11, pp. 1663–1666, 2012.

[199] U. Çilingiroğlu and S. İpek, "A zero-voltage switching technique for minimizing the current-source power of implanted stimulators," *IEEE Trans. Biomed. Circuits Syst.*, vol. 7, no. 4, pp. 469–479, 2013.

ABOUT THE AUTHORS

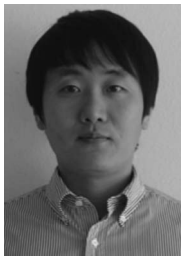

Sohmyung Ha (Member, IEEE) received the B.S. (*summa cum laude*) and M.S. degrees in electrical engineering from the Korea Advanced Institute of Science and Technology (KAIST), Daejeon, South Korea, in 2004 and 2006 and the M.S. and Ph.D. degrees in bioengineering from the University of California San Diego, La Jolla, CA, USA, in 2015 and 2016, respectively.

From 2006 to 2010, he worked as an Analog and Mixed-Signal Circuit Designer at Samsung Electronics Inc., Yongin, Korea, where he was a part of the engineering team responsible for several of the world best-selling multimedia devices, smartphones and TVs. As of September 2016, he joins New York University Abu Dhabi, UAE, as an Assistant Professor in Electrical Engineering. His research aims at advancing the engineering and applications of silicon-integrated technology interfacing with biology in a variety of forms ranging from implantable biomedical devices to unobtrusive wearable sensors.

Dr. Ha received the Fulbright Fellowship from 2010 to 2012, and the Engelson Ph.D. Thesis Award from the Department of Bioengineering, University of California San Diego, in 2016.

Abraham Akinin (Student Member, IEEE) was born in Caracas, Venezuela. He received the B.S. degree in biomedical engineering and physics from the University of Miami, Coral Gables, FL, USA, in 2010. He is currently working toward the Ph.D. degree at the Bioengineering Department and the Institute for Neural Computation, University of California San Diego, La Jolla, CA, USA.

His research interests include design of closed-loop neuroprosthetics and biomedical instrumentation to restore sensory and cognitive function.

Jiwoong Park (Student Member, IEEE) received the B.Sc. degree in electronic and computer engineering from Hanyang University, Seoul, South Korea, in 2012 and the M.S. degree in electrical and computer engineering from the University of California San Diego (UCSD), La Jolla, CA, USA, in 2014, where he is currently working toward the Ph.D. degree.

His research interests include the design of ultralow power body area network systems and the design of miniaturized wireless power transfer systems for biomedical implants.

Chul Kim (Student Member, IEEE) received the B.S. degree from Kyungpook National University, Daegu, South Korea, in 2007 and the M.S. degree from Korea Advanced Institute of Science and Technology (KAIST), Daejeon, South Korea, in 2009, both in electrical engineering. He is currently working toward the Ph.D. degree in the Bioengineering Department, University of California San Diego, La Jolla, CA, USA.

During 2009-2012, he worked for SK HYNIX as a Power Circuitry Designer for DRAM. His research focuses on designing micropower integrated circuits and systems for biomedical applications and brain-machine interfaces.

Hui Wang (Student Member, IEEE) received the B.Sc. degree in microelectronics and the S.M. degree in circuits and systems from Shanghai Jiao Tong University, Shanghai, China, in 2009 and 2012, respectively. He is currently working toward the Ph.D. degree in electrical and computer engineering at the University of California San Diego (UCSD), La Jolla, CA, USA.

His research interests include the design of fully integrated low-power acquisition platforms for biomedical and implantable applications, ultralow-power clock generations, and energy-efficient mixed-signal integrated circuits for long-term environmental and medical monitoring systems.

Christoph Maier (Member, IEEE) received the Diplom-Physiker degree from the University of Heidelberg, Heidelberg, Germany, in 1995 and the Dr.sc.techn. degree in electrical engineering from the Swiss Federal Institute of Technology Zurich, Zurich, Switzerland, in 2000.

After time in industry, he joined the Integrated Systems Neuroengineering Laboratory, University of California San Diego, La Jolla, CA, USA, as a Postdoctoral Researcher in 2010. His main research interests are interfaces for electrophysiological signals and modeling neural networks in analog VLSI.

Patrick P. Mercier (Member, IEEE) received the B.Sc. degree in electrical and computer engineering from the University of Alberta, Edmonton, AB, Canada, in 2006 and the S.M. and Ph.D. degrees in electrical engineering and computer science from the Massachusetts Institute of Technology (MIT), Cambridge, MA, USA, in 2008 and 2012, respectively.

He is currently an Assistant Professor in Electrical and Computer Engineering at the University of California San Diego (UCSD), La Jolla, CA, USA, where he is also the Co-Director of the Center for Wearable Sensors. His research interests include the design of energy-efficient microsystems, focusing on the design of RF circuits, power converters, and sensor interfaces for miniaturized systems and biomedical applications.

Prof. Mercier received a Natural Sciences and Engineering Council of Canada (NSERC) Julie Payette fellowship in 2006, NSERC Postgraduate Scholarships in 2007 and 2009, an Intel Ph.D. Fellowship in 2009, the 2009 ISSCC Jack Kilby Award for Outstanding Student Paper at ISSCC 2010, a Graduate Teaching Award in Electrical and Computer Engineering at UCSD in 2013, the Hellman Fellowship Award in 2014, the Beckman Young Investigator Award in 2015, the DARPA Young Faculty Award in 2015, and the UCSD Academic Senate Distinguished Teaching Award in 2016. He currently serves as an Associate Editor of the IEEE Transactions on Biomedical Circuits and Systems and the IEEE Transactions on Very Large Scale Integration, and is coeditor of *Ultra-Low-Power Short-Range Radios* (New York, NY, USA: Springer-Verlag, 2015), and *Power Management Integrated Circuits* (Boca Raton, FL, USA: CRC Press, 2016).

Gert Cauwenberghs (Fellow, IEEE) received the M.Eng. degree in applied physics from the University of Brussels, Brussels, Belgium, in 1988 and the M.S. and Ph.D. degrees in electrical engineering from the California Institute of Technology, Pasadena, CA, USA, in 1989 and 1994, respectively.

Currently, he is a Professor of Bioengineering at the University of California San Diego, La Jolla, CA, USA, where he codirects the Institute for Neural Computation, participates as a member of the Institute of Engineering in Medicine, and serves on the Computational Neuroscience Executive Committee of the Department of Neurosciences graduate program. Previously, he was Professor of Electrical and Computer Engineering at Johns Hopkins University, Baltimore, MD, USA and Visiting Professor of Brain and Cognitive Science at the Massachusetts Institute of Technology, Cambridge, MA, USA. He cofounded and chairs the Scientific Advisory Board of Cognionics Inc. His research focuses on micropower biomedical instrumentation, neuron–silicon and brain–machine interfaces, neuromorphic engineering, and adaptive intelligent systems.

Dr. Cauwenberghs received the National Science Foundation Career Award in 1997, the Office of Naval Research (ONR) Young Investigator Award in 1999, and the Presidential Early Career Award for Scientists and Engineers in 2000. He was Francqui Fellow of the Belgian American Educational Foundation. He was a Distinguished Lecturer of the IEEE Circuits and Systems Society in 2002–2003. He served IEEE in a variety of roles including as General Chair of the IEEE Biomedical Circuits and Systems Conference (BioCAS 2011, San Diego), as Program Chair of the IEEE Engineering in Medicine and Biology Conference (EMBC 2012, San Diego), and as Editor-in-Chief of the IEEE Transactions on Biomedical Circuits and Systems.